10 The MINERνA Detector

10.1 Overview of Detector Design

For MINERνA to meet its physics goals, the detector must break new ground in the design of high-rate neutrino experiments. With final states as varied as high-multiplicity deep-inelastic reactions, coherent single-π^0 production and quasi-elastic neutrino scattering, the detector is a hybrid of a fully active fine-grained detector and a traditional calorimeter.

At the core of the MINERνA design is a solid scintillator-strip detector, similar in principle to the recently commissioned K2K SciBar [156]. The plastic inner detector serves as the primary fiducial volume, where precise tracking, low density of material and fine sampling ensures that some of the most difficult measurements can be performed. These include multiplicity counting in deep-inelastic scattering, tracking of photons, detection of recoil protons in low-Q^2 quasi-elastic events, and particle identification by dE/dx. A side view of the detector is shown in Figure 43.

The scintillator detector cannot contain events due to its low density and low Z, and therefore, the MINERνA design surrounds the scintillator fiducial volume with sampling detectors. At the low energies needed to study cross-sections of interest to neutrino-oscillation searches, many of the events contain sideways- and backward-going particles, so these sampling detectors extend to the sides, and even to the upstream part of the detector, where they also serve as high A targets for study of nuclear effects. Finally, it is important to contain or measure the final-state muon in charged-current events, and for this purpose, the outer side detector of MINERνA is a magnetized toroid. Energetic muons at smaller angles will enter the MINOS near detector, where their momentum can be measured magnetically and/or by range.

Except for the upstream veto, the entire MINERνA detector is segmented transversely into an inner detector with planes of solid strips and an outer picture frame magnetized toroid (OD). For construction and handling convenience, a single plane of MINERνA incorporates both the inner detector and OD, which serves as the support structure. Two planes of scintillator are mounted in one frame, called a "module", as illustrated in Figures 45,46. There are three distinct orientations of strips in the inner detector, offset by 60°, and labelled X, U, and V.

A single module of the MINERνA active target has two X layers to seed two-dimensional track reconstruction, and one each of the U and V layers to enable a three-dimensional reconstruction of tracks. The 60° offset makes the hexagon a natural transverse cross-section for the detector. As shown, the scintillator strips extend the full length of the hexagon and range between 205 and 400 cm in length. The toroid steel/absorber is 10 cm thick in the veto; The magnetic properties of the OD are discussed in Section 10.4.

The center of the detector is the fully active inner detector (ID), whose plastic core represents the fiducial volume for most analyses in MINERνA. Calorimetric detectors in the central region of the detector are constructed by inserting absorber between adjacent planes, also shown in Figures 45,46. Lead alloy absorbers, 30 cm from the edge of the ID and 0.2 cm thick, are inserted between layers of scintillator and at the front of each module to serve as a side electromagnetic calorimeter. This part represents the largest part of the detector in length, and the outer calorimeter surrounding the fully active planes are the largest part of the detector in mass.

The inner detector is surrounded by the picture frames of absorber and scintillator strips that make up the outer detector (OD). The OD consists of six "towers" (one sixth of a hexagon). Note that the strips in the OD run only in one direction, in the bend plane of the magnetic field. Three-dimensional

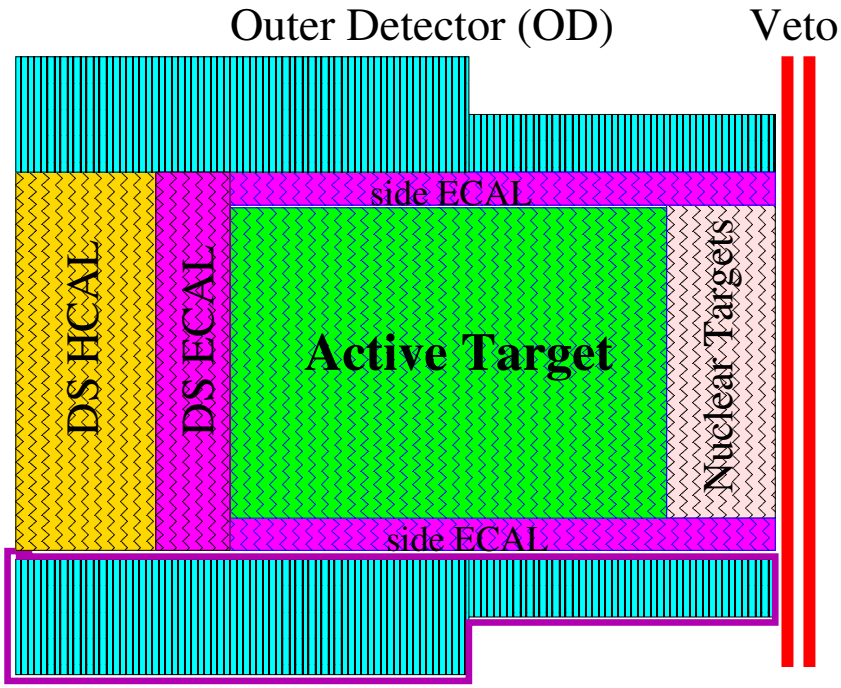

Figure 43: A side view schematic of the MINERνA detector

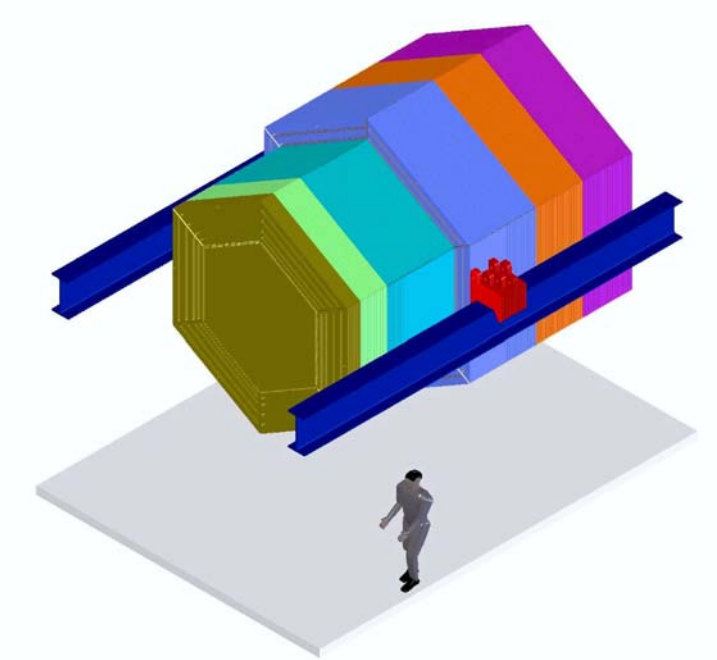

Figure 44: Outline of MINERνA detector to illustrate shape and scale. The veto wall is omitted for clarity.

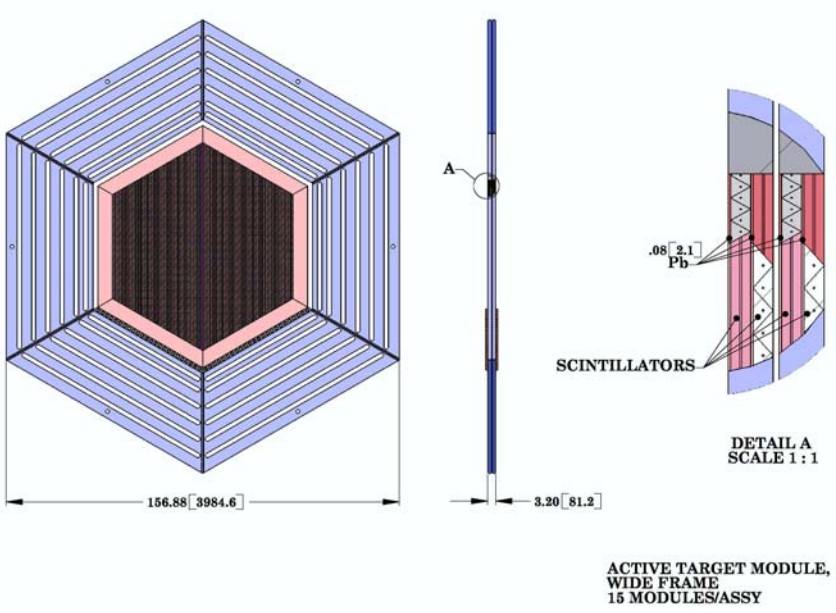

Figure 45: View of downstream active detector region. An expanded view of the area near the inner-outer detector interface is shown on the right.

tracks must therefore be matched from the inner detector and extrapolated outwards for an energy measurement or muon momentum measurement. A complication of the design is illustrated by the fact that the inner detector strips, which range in length from 120 to 240 cm, end inside the OD, and therefore bundled WLS fibers in a so-called "snout" must travel through the gap between the OD planes of each module to the detector edge. Note also the gaps for the muon toroid coil on the inner surfaces of the "5 O'clock" and "7 O'clock" sides of the OD. Magnetic flux will be isolated in each region of the OD, and will be prevented from leaking into the inner detector by gap between steel HCAL absorbers and the OD. The scintillator strips in the towers are square, with 1.9 cm sides, and arranged in rectangular layers of two (Figure 57).

In the inner detector, MINERνA's sensitive elements are extruded triangular scintillator strips, 1.7 cm height with a 3.3 cm base, with embedded wavelength-shifting fibers (details given in Section 10.2.1). To improve coordinate resolution while maintaining reasonably large strips, these elements are triangular and assembled into planes (Figure 56); this allows charge-sharing between neighboring strips in a single plane to interpolate the coordinate position.

The most up- and down-stream detectors are the hadronic calorimeters (HCALs) with 2.5 cm absorbers, one per plane downstream and one per module upstream, as shown in Figures 47 and 48. Next are the electromagnetic calorimeters, as shown in Figures 49 and 50. The electromagnetic calorimeters (ECALs) have 0.2 cm Pb alloy absorbers downstream, one per plane, and 0.8 cm Pb alloy absorbers upstream, one per module. The absorber only overlaps the inner detector and not the outer detector where it would represent a negligible fraction of the absorber material. The fine granularity of the ECAL ensures excellent photon and electron energy resolution as well as a direction measurement for each. In Figure 43, the upstream HCAL and ECAL are labeled as one device called "nuclear targets" since these planes serve all three purposes.

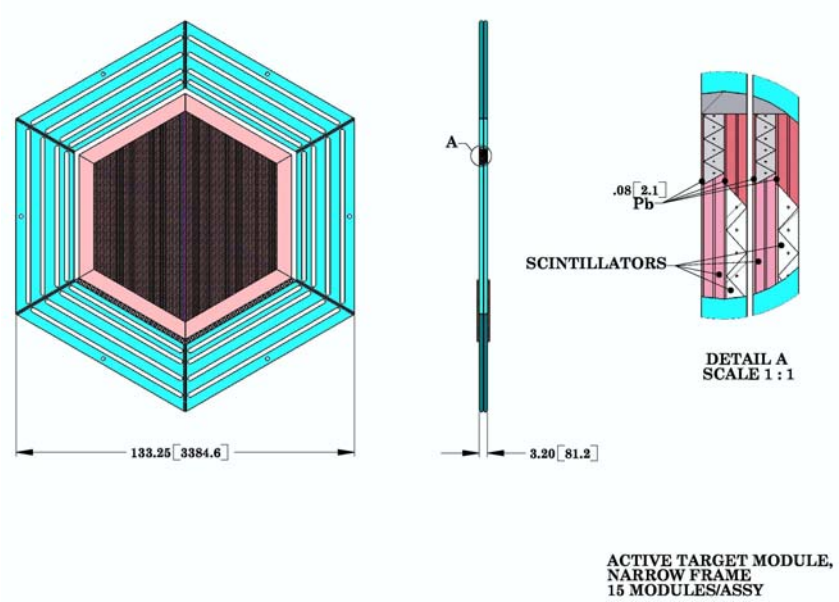

Figure 46: View of an upstream active detector module. An expanded view of the area near the inner-outer detector interface is shown on the right.

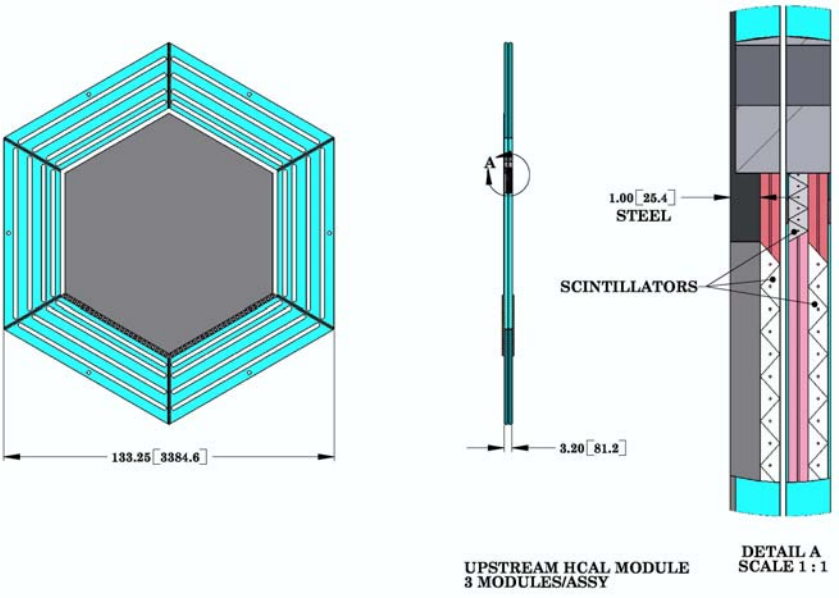

Figure 47: View of an upstream hadron calorimeter module. An expanded view of the area near the inner-outer detector interface is shown on the right.

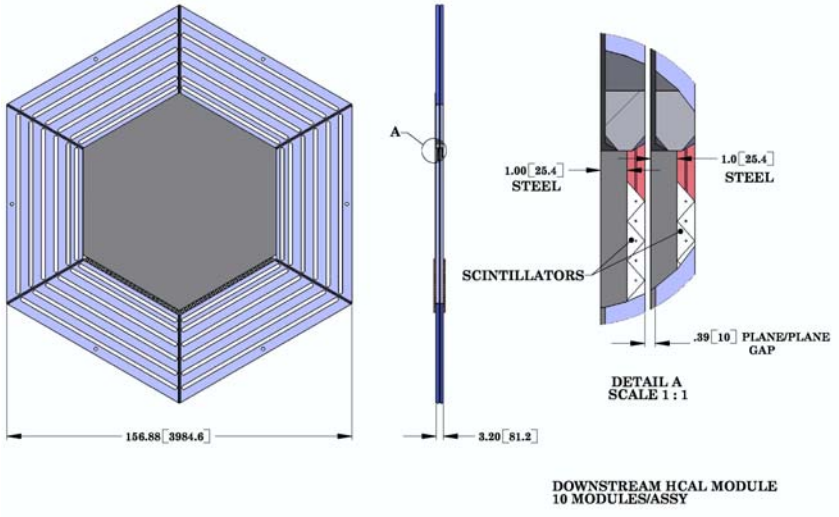

Figure 48: View of a downstream hadron calorimeter module. An expanded view of the area near the inner-outer detector interface is shown on the right.

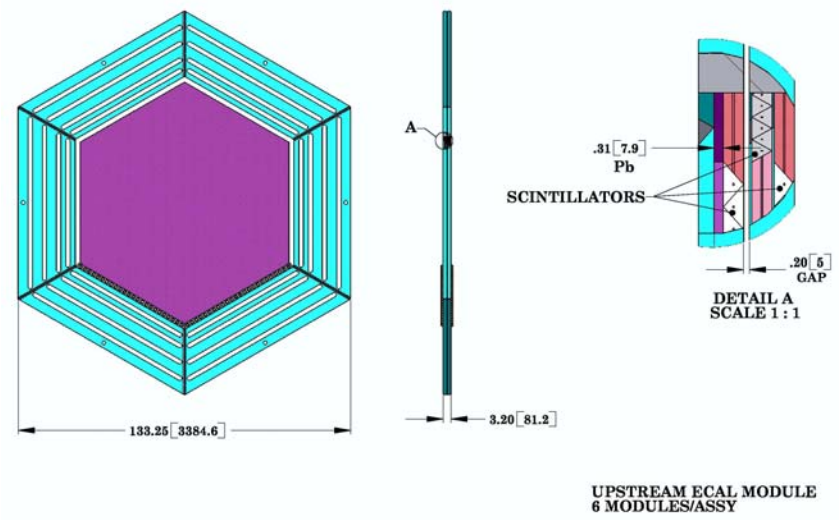

Figure 49: View of an upstream electromagnetic calorimeter module. An expanded view of the area near the inner-outer detector interface is shown on the right.

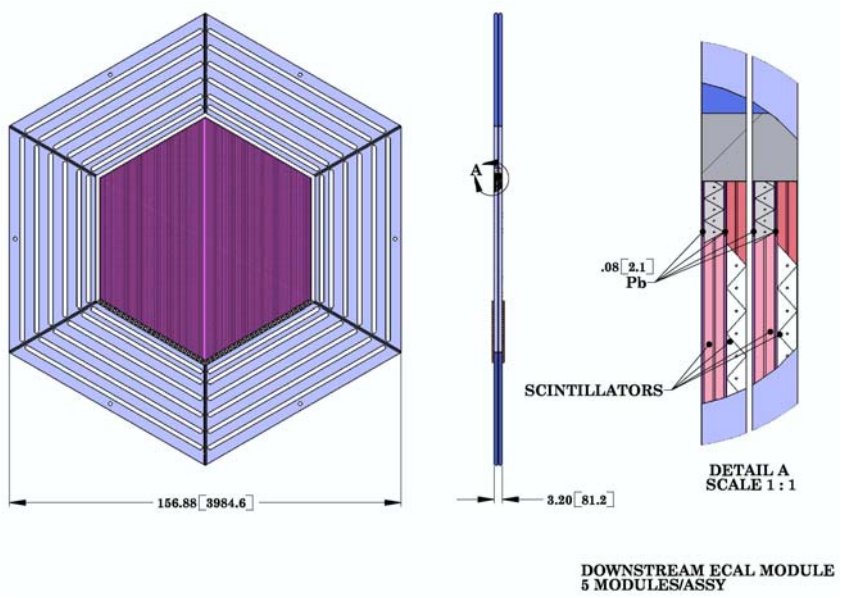

Figure 50: View of an downstream electromagnetic calorimeter module. An expanded view of the area near the inner-outer detector interface is shown on the right.

Note that MINERνA is, by design, entirely modular along the beam direction. Individual elements may be easily lengthened or shortened by omitting modules from the design or adding new modules. Hence, it would be easy to add a muon range stack at the downtream end of the MINERνA detector, if that should be required at a future date.

10.2 Scintillator

10.2.1 Scintillator extrusions

Particle detection using extruded scintillator and optical fibers is a mature technology. While in terms of size, MINERνA pales in comparison to MINOS, our system is similar in scale to other successful applications in the K2K SCIBAR detector, CDF plug calorimeter, and CMS HCAL. We have opted for a 1.7 cm height, 3.3 cm base triangular extrusion cross-section for the inner detector planes (Figure 51); this geometry allows refinement of spatial coordinates based on charge-sharing between adjacent strips (Figure 56). For the outer detector, strips will be square in cross-section, 1.9 cm on a side, arranged in rectangular groups of two (Figure 57).

Scintillator elements will be produced by the Northern Illinois Center for Accelerator and Detector Development (NICADD) at Northern Illinois University (NIU). NIU physicists and mechanical engineers have formed a collaboration to support development of the next generation of detectors at the Fermilab Scintillator Detector Development Laboratory. NICADD/NIU fully purchased and is sole owner of the NICADD/Fermilab extruder at the heart of the scintillator laboratory. NICADD and Fermilab jointly operate the extruder to ensure that the HEP community has access to affordable extruded scintillator. NICADD/NIU personnel have been responsible for commissioning the extruder; simulations, production, and prototyping of dies associated with specific detectors; and production of extrusions for

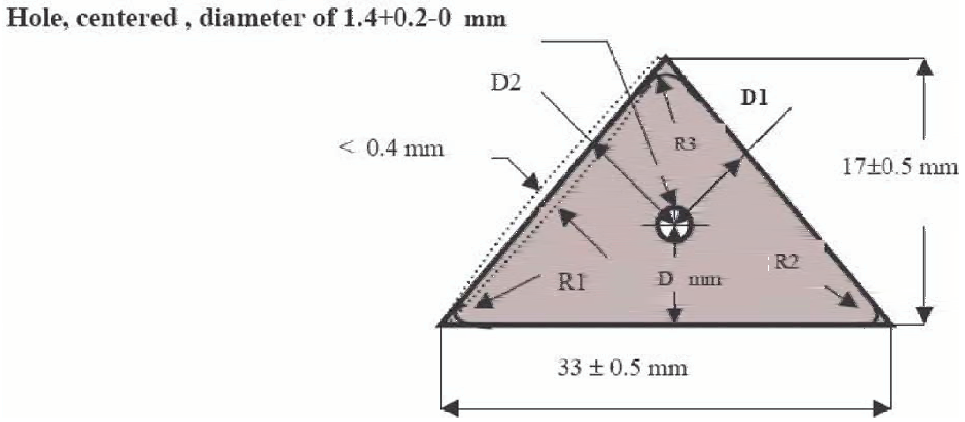

Figure 51: Specification for MINERνA's inner-detector scintillator extrusions.

prototypes and detector construction.

The key element in producing extruded scintillator is the metal die used to shape the final scintillator cross-section. Historically, development of the die has been more of an art than a science, marked by repeated redesigns and dependent on the die-maker's experience. To refine this process, NIU's mechanical engineering department formed a group to design dies through advanced computing and simulation techniques.

Figure 52 shows the die developed for MINERνA's first triangular extrusion prototypes in Summer 2004. A small number of these prototypes, with holes through the center of the bar for fiber insertion, were used successfully to detect cosmic-ray muons as part of our "Vertical Slice Test" (see Section 11.5). Figure 53 shows several of the first prototypes.

On-going R&D is focused on perfecting the extruded hole dimensions for a closer fit and more uniform light collection, which will improve MINERνA's response and sensitivity.

The 23 metric tons of extruded scintillator for the full MINERνA design will require a production run of approximately 18 weeks. Quality control procedures to ensure the light-yield of the finished product will be maintained by NIU personnel throughout production.

10.2.2 Wavelength-shifting fibers

MINERνA will read-out only one end of its wavelength-shifting (WLS) fibers. To maximize light collection, we will make the unread end of each fiber reflective using techniques developed at Fermilab (the expected improvement in light collection is quantified in Section 11.3). "Mirroring" consists of 3 steps: polishing the end to be mirrored, depositing the reflective surface on the fibers (a process called sputtering), and protecting the mirrors.

The fibers will be delivered in batches from one fiber preform. An automated fiber scanner available at Fermilab will determine if the attenuation length of the fiber is acceptable.

A technique called ice polishing is used to prepare the fibers prior to applying the reflective coating. Ice polishing can give a very good finish to many fibers at once. This technique is described in detail in [161].

The reflective coating is applied in a vacuum system dedicated to optical fiber mirroring at Fermilab. The number of fibers that can be sputtered per load depends on the diameter, but typically 1000–2000

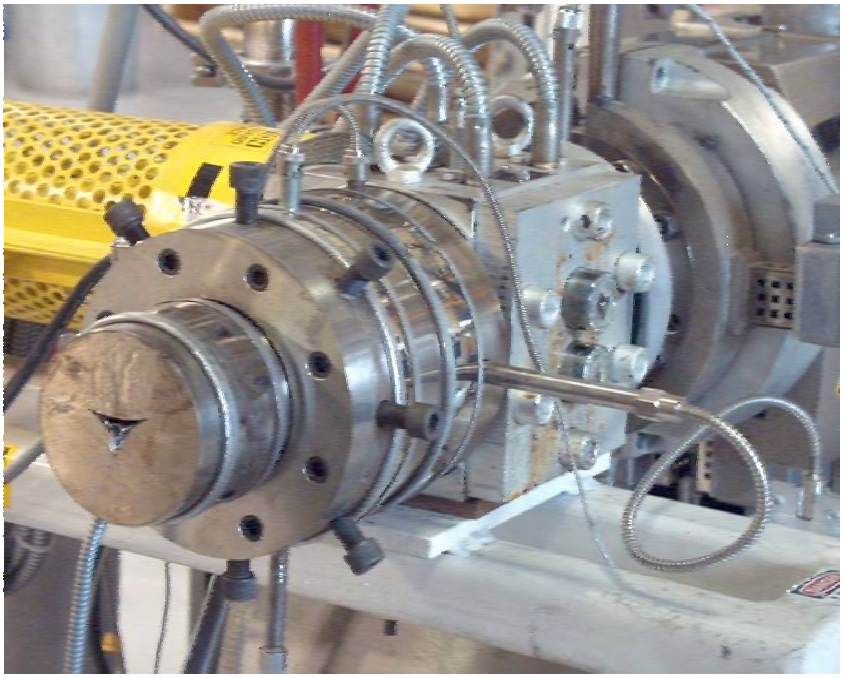

Figure 52: Die developed to produce scintillator bar prototypes for MINERνA's vertical slice test, mounted to the front of the NICADD extruder. The die is designed, using a finite-element thermal simulation, so the extruded bar will cool into the desired shape in Figure 51.

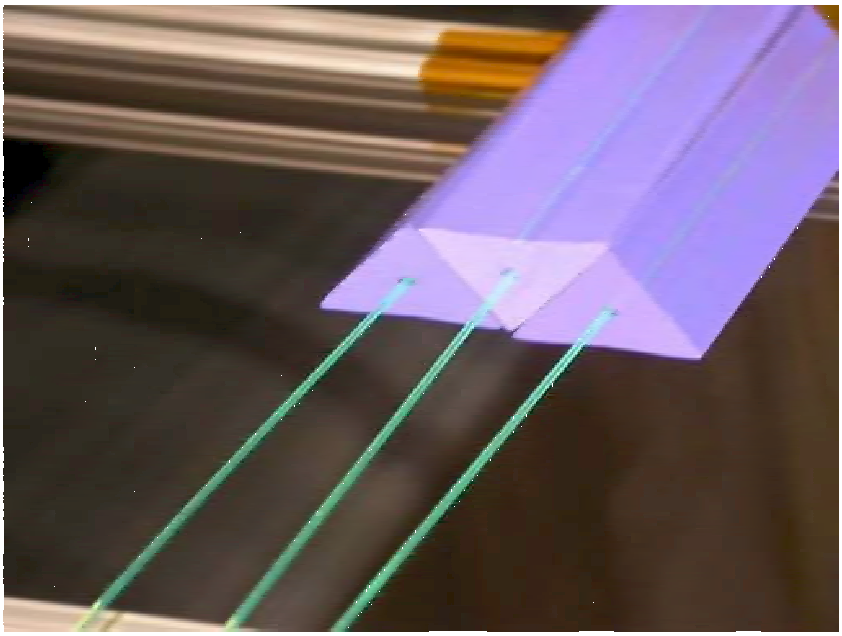

Figure 53: Prototype MINERνA scintillator bars, with wavelength-shifting fibers inserted.

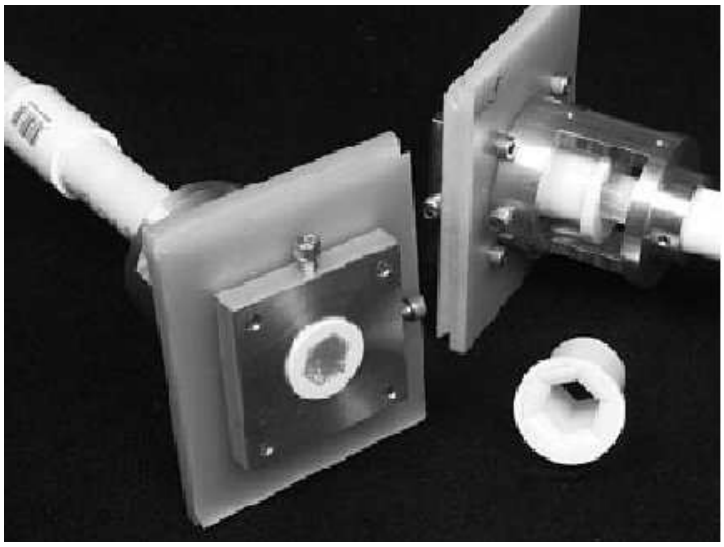

Figure 54: A urethane fixture in an aluminum/G10 frame for holding optical fibers during ice polishing.

fibers per pumpdown per unit can be coated. A 99.999% chemically pure aluminum coating is a applied for good reflectivity. The coating is approximately 2500 Angstroms thick and is monitored using an oscillating quartz crystal sensor device. The aluminized ends are protected with a coat of epoxy.

After this process, MINERνA will do a destructive measurement of the mirror reflectivity with production fibers, similar to one developed in the CDF plug upgrade. Light output is measured through the unmirrored end of a fiber with ultra-violet light incident on the fiber near the mirrored end. Then, the mirrored end is cut off at 45°, painted black, and the light yield is remeasured with the UV light at the same place. CDF measured an average mirror reflectivity of 90%, with 5.4% RMS variation [162].

10.2.3 Scintillator plane design

Scintillator extrusions, optical fibers, and optical connectors are assembled into scintillator planes. There are two varieties of scintillator assemblies: inner-detector (ID) planes and outer-detector (OD) towers. The planes incorporate light-tight skins and edge pieces; they also route the fibers from the ends of the scintillator strips to the outside of the detector. This task's interface with the optical readout system is at the optical connectors between green wavelength-shifting fibers and clear optical cables.

The ID planes are hexagonal assemblies of 128 strips in a single view (X, U or V). An ID plane is also called a "hex". The six OD towers of a complete detector module each consist of four or six OD modules, or stories, stacked radially outward. A single OD module has 2 roughly square strips nested to make a rectangular package. (We also considered a variant designed for improved resolution with four triangular strips, but we consider the 2 square strip design here as the default.) The layout of the ID and OD is shown schematically in Figure 55. A schematic cross-section of a hex is shown in Figure 56, while the cross-section of an OD scintillator module is shown in Figure 57.

The plane design is inspired by the successful MINOS near detector scintillator module assembly [152], but a few modifications are required to meet MINERνA's needs. Most significantly, the aluminum skins from the MINOS modules represent too much high-Z material for the MINERνA tar-

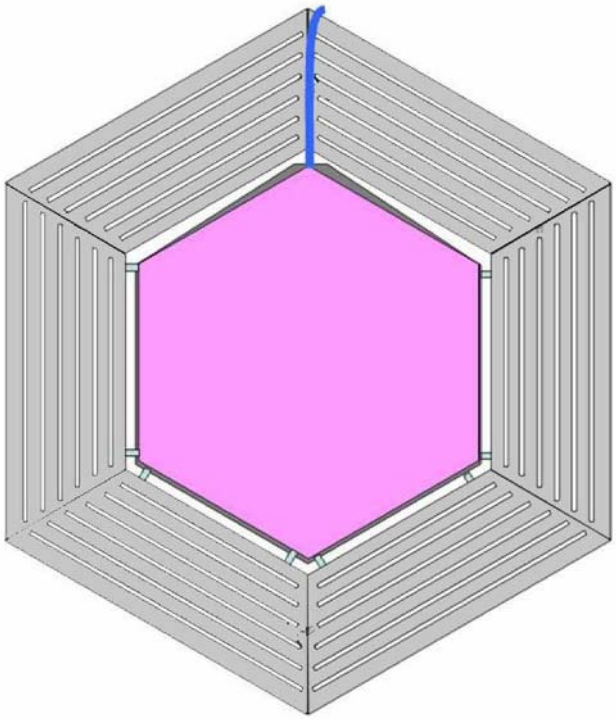

Figure 55: Schematic of a full (inner + outer) detector plane. The hexagonal ID plane is surrounded by six trapezoidal OD towers, each consisting of six OD modules, or stories.

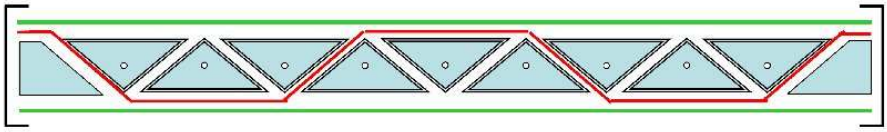

Figure 56: Schematic cross-section of an ID plane, or hex, assembly. The triangular scintillator strips are blue, the outer skins green, the inner web is red, and the outer edge seals are black.

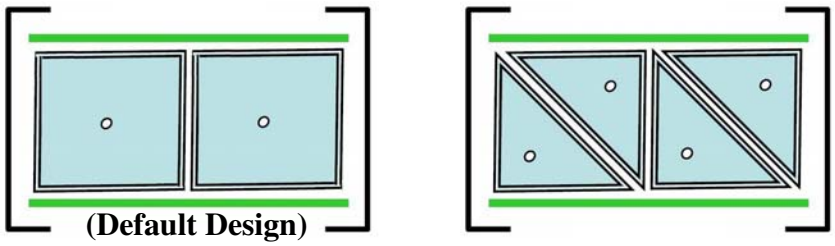

Figure 57: Schematic cross-section of a single OD tower scintillator module, or story. The design with two roughly square extrusions (left figure) is the default; we also considered a triangular design (right figure). The extrusions are blue, the outer skins are green, and the outer edge seals are black.

get region and are replaced with new materials. In addition, the triangular strip design uses an axial hole rather than a groove for better dimensional tolerances.

For light tightness and rigidity, each plane is wrapped in skins made from commercially laminated black Mylar layers with embedded threads of Kevlar. These skins are glued to form the assemblies. A web layer of the skin material is routed between the triangles to provide flat gluing surfaces and a robust connection between the outer skins. The edges of the modules contain small triangular extruded plastic strips to provide square edges to facilitate light sealing with a flexible black extruded PVC edge seal. The ends of the planes contain plates, called manifolds, made from black foamed PVC. On the readout end, these manifolds are partially grooved to route the fibers to their exit points at the end of the assembly. The green fibers are extended past the end of the inner hex in a flexible snout to the outside of the detector where a DDK optical connector is used to make a transition to a clear optical cable.

For eventual installation in the steel detector frames, the scintillator assemblies will have stamped and folded metal brackets attached at six locations around the perimeter of the hex. These tabs will be welded to the steel during detector module assembly. This process is similar to the H-clip mounting technique developed for the MINOS detectors. Next to the flexible snout a small guard piece ensures the fibers are not crushed. Finally, the lead foils of the side ECAL are glued to the skins at the outer radius of the planes.

Assembly of MINERνA scintillator planes will be undertaken at both Hampton University and the College of William and Mary. Both programs have extensive experience in detector production. Since the two institutions are located less than 25 miles from each other (and less than 15 miles from JLab), they form a natural team for undertaking a joint detector production program. This team will benefit from a collaborative prototyping program, and the joint set-up costs are minimal for this project.

All of the parts other than the scintillator strips, lead sheets, mirrored fibers, and optical connectors will be procured or fabricated by these two institutions. Bulk purchasing responsibilities will be shared by the two institutions, according to the particular strengths and experience of each.

10.2.4 Scintillator plane assembly

The module assembly process for MINERνA planes are based on those used in MINOS project. Labor requirements for prototyping and assembling the MINERνA scintillator planes are estimated from extrapolation of the as-realized MINOS far detector scintillator module production. The labor model for this construction is based on a mixture of full-time mechanical technicians and undergraduates, which is the same as employed for MINOS at University of Minnesota.

An overview of the four-day scintillator plane assembly process is briefly summarized here. Prior to the first day, we receive scintillator strips, fibers, optical connectors, and the various parts and supplies for construction. In the first day of the process, we initially cut the scintillator to length. Each strip of scintillator will come bar coded for tracking purposes. After that, the lower skin, fiber routing trays, survey fiducials, and lower strips are laid into position. A layer of adhesive is applied to the gaps between the strips and the web layer is positioned. We then cover the assembly with a vacuum seal and cure it overnight. On the second day, we lay the upper strips, insert fibers, apply a layer of glue, and lay the top skin. The assembly is again covered in a vacuum seal and cured overnight. On the third day we polish connectors, perform initial quality assurance, fix bad fibers, seal the ends, and glue a layer lead to the skin. The assembly is then covered a third time in a vacuum seal and cured overnight. The last day involves final quality assurance, fixing possible light leaks, and packaging for shipment. Each scintillator assembly's response will be mapped after shipping to Fermilab, after mounting in a detector

module frame, as described in Section 10.3.4.

MINERνA requires a total of 196 hexes and 1612 OD modules. We will produce an additional 12 hexes and 89 OD modules as spares. We assume 3% wasted components during production so the total part counts corresponds to 214 ID and 1612 OD assemblies.

10.3 Detector Modules

10.3.1 Module frames

The basic frame shape is shown in Figure 55, and is about 4.3 meters tall. Each frame serves several purposes: to hold the scintillator composing the inner detector, to serve as a skeleton for the outer detector, to provide a magnetic field outside the inner detector, and to support the lead for the electromagnetic calorimeter. Each frame holds two layers of scintillator, and there are a total of 98 frames. Because the detected particles produced in the fiducial volume will be lower-energy in the most upstream part of the detector, the thickness of the outer detector will be about 60 cm smaller in that region. The thickness of individual towers is 56 cm for the upstream section and 87 cm for the downstream section.

A number of factors were considered in the outer-detector frame design: material, thickness, production of the hex (from single plate or welded individual plates), and construction of slots. We discuss each of these in turn, with attention to factors that will affect construction and robustness of the resulting calorimeter.

Because the frame will be magnetized, it must be made of a material with good magnetic properties. We have chosen soft steel with the specifications used by MINOS. This is basically AISI 1006 (less than 0.06% C), with some additional requirements on other impurities. This alloy is not a stock item and will require a few month lead time to be produced.

We considered making the hexagon from a single plate, but the required width (about 3.7 meters) is larger than what is generally available, and cutting the center out would involve a great deal of waste (and cost). Instead, we will make each tower separately and weld the plates together at Fermilab. The individual towers are about 2.2 meters long and nearly one meter wide.

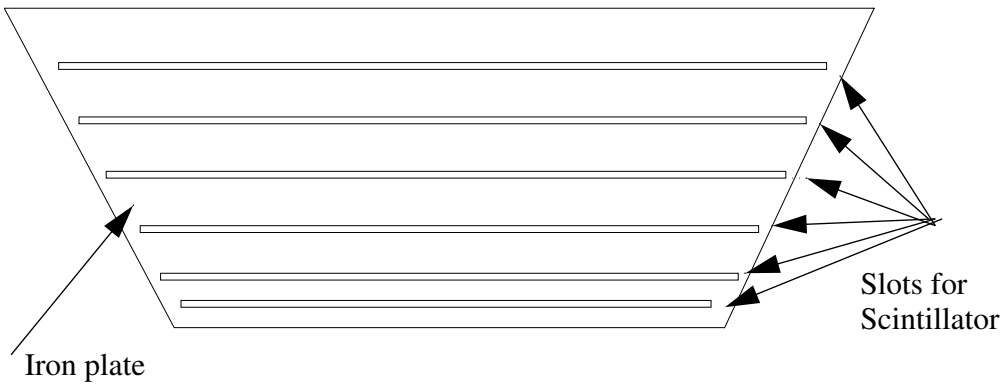

Figure 58: Schematic of one tower showing scintillator placement.

Each tower has six slots, as shown in Figure 58, nominally 1.6 cm (5/8 inch) wide to hold the scintillator. Our initial plan was to have each hexagon hold one layer of scintillator, so the plates would be approximately 1.6 cm thick. After discussion with the steel manufacturer and machine shops, we have instead decided to use 3.8 cm (1.5 inch) thick plates. From the steel production view, the thinner

plates would be difficult to make flat, and mills will charge more to make it. Cutting the slots in such a thin material would lead to warping of the plates, and welding would also be more problematic. While none of these problems were insurmountable, going to a thicker plate made the design less prone to problems and less expensive.

Cutting slots in the plate is a time consuming (and hence expensive) procedure. The cheapest technique appears to be flame cutting. This can be done to a precision of about 1.6 mm (1/16 inch), which is adequate for our purposes. It will require a somewhat wider slot (about 2 cm), which will necessitate increasing the width of the tower slightly to keep the same absorber thickness. This method will likely cause considerable warping of the plates (more than 1 cm) and change the magnetic properties near the cuts. Annealing the plates after cutting will both flatten the plates and give more uniform magnetic properties.

The normal method of handling plates of this size is with magnets. In order to avoid magnetizing the plates, we will need to cut some holes to allow the plates to be easily moved with a crane. In addition, holes will be drilled and tapped to allow attachment of the lead plates.

The number (588) and size (about 225 kg each) of these plates, as well as the need to flame cut the slots, puts their construction beyond the capabilities of a university shop.

Once the plates are constructed, they will be shipped to Fermilab for final assembly. The plates require welding only at the ends of the joints for mechanical strength. We do not expect the magnetic properties to be significantly affected by the small gap between plates. A finite element analysis showed the frame will sag less than 0.1 mm.

We have obtained non-binding quotes from Metals USA, Inc. for the steel and machining needed for this frames. The estimated delivery time is 6-8 months.

10.3.2 Calorimeters

The calorimeters are in three distinct regions: upstream of the active target, around the active target (the outer detector), and downstream of the active target. The upstream calorimeter will also provide a variety of nuclear targets (carbon, iron, lead).

Upstream calorimeters and nuclear targets To study differences in neutrino scattering from different nuclei, three nuclear targets, carbon, iron, and lead, will be mounted on the upstream side of the active target area. Scintillator planes identical to the central detector modules will be interleaved with the passive target/absorber material. The mass of the lead and iron will each be about one ton, and the carbon target in this region will be about half a ton. The nuclear targets will also serve as absorbers for the upstream calorimeter.

Our proposed arrangement, illustrated in Figures 49 and 47, is to have planes of a single material in this area. However, to reduce systematic errors in comparisons across different nuclear targets, we are considering using partial planes of multiple materials in a single layer for at least some modules. More studies are required to finalize this decision. The decision should not significantly affect the estimated cost because it involves only the arrangement of the layers.

Side calorimeters To provide electromagnetic calorimetry for particles exiting the sides of the fully-active central region, lead plates will be mounted on the frames and extend over part of the central scintillator region. Smaller plates will be mounted between the two scintillator layers contained in each frame. The plates will be approximately 2 mm thick. Pure lead plates are not strong enough to support

their own weight when attached with screws to the main frame, so we will use a Pb-Ca-Sn alloy which is considerably stronger than pure lead. Tests performed at Rochester with this alloy have confirmed that its strength is adequate.

The hexagonal frame also serves as the outer detector, with layers of iron and scintillator (as discussed above). The frame will serve as a ranger for lower energy particles and as a muon detector.

Downstream calorimeters The downstream electromagnetic calorimeter (ECAL) and hadron calorimeter (HCAL) are simple variations of the basic detector module - identical scintillator planes, but separated by absorbing material. The ECAL consists of sheets of lead alloy 2 mm (5/64 inch) thick (the same material as used for the side ECAL), which cover the entire hex frame, with layers of scintillator between the sheets. The HCAL will consist of 2.5 cm (1 inch) steel plates, also covering the entire frame, also with layers of scintillator between the plates.

10.3.3 Module assembly

As shown in Figures 45–50, MINERνA modules consist of two outer detector frames, two, three or four hex planes of scintillator in assemblies and 24 or 36 outer detector scintillator modules as described in Section 10.2.3, and the appropriate calorimetric absorbers for the type of modules. The completed assembly serves as a single structural unit of the detector which is assembled above ground, transported to the NuMI near hall and there installed on the detector support frame.

In brief, the assembly procedure consists of the following steps. Two outer detector steel frame trapezoids are arranged on strongbacks on a frame-table and skip welded into OD frames; lifting and mounting fixtures and frame fiducials are welded onto the frames; and necessary steel absorbers are welded or lead or graphite absorbers are screwed into the frame. At this point, the frame may be flipped to allow for scintillator installation if absorbers were screwed onto the frame face. Then, the hexagonal scintillator planes and OD modules with their associated fiber cable "snouts" are arranged onto the frame and tack welded into place on each frame. One of the two frames in the module is flipped and laid onto the other where the two are joined together with a module joining plate and the top strongback is removed. The completed module with its remaining strongback is then ready for mapping, and eventually for installation.

This work will be led by university (Rochester) technicians, resident at Fermilab, and will be assisted by FNAL welders and physicists who will run the mapping process. We plan to house the assembly facility in the New Muon Lab at FNAL because of good crane coverage and significant available floor space. Figure 59 shows technicians doing similar work during assembly of the MINOS near detector.

10.3.4 Module response mapping

Within MINERνA, two hexagonal planes of scintillator are physically combined into a structure called a "pan"; two pans are combined into inner-detector "modules". We will use a source scanner for quality control of each module before final installation and to map the local response of the detector. The source scanner moves a collimated source over the the broad face of the scintillator module, creating scintillation light at known positions.

Variation in local response is dominated by the attenuation length of wavelength-shifting fiber. A smaller contribution to the non-uniformity (1–2%) is due scintillator itself. The primary goal of mapping

Figure 59: Module assembly work for MINOS, closely analogous to the MINERνA initial (left) and final (right) assembly steps, being performed by technicians at the New Muon Lab. Note the use of the Lab's crane and floor space.

modules with the scanner is to measure the attenuation length of the fibers in each pan. The overall gain for each channel (including PMT response and loss in optical connections) will be determined with cosmic-ray and neutrino-induced muons in the experimental hall. Since most damaged fibers can be diagnosed visually, we will check the fibers for before and after installation. Hence the purpose of the scanner is to map the local response, not to calibrate gains or identify broken fibers.

A similar system, pictured in Figure 60, was employed used by MINOS. Our system will be built and operated based on the MINOS design. In the MINOS scanner, the short axis moves using a lead screw, and the long axis moves using using a rack and pinion system. The pinion gear and gear rack were manufactured by Martin Gear. The scanner moves at a rate of 0.15 m/sec along the short axis and 1 m/s along the long axis. The motors on both axes use servo motors made by Aerotek. Both motors employ planetary speed reducers (10:1 for the long axis, 4:1 for the short axis) made by Minarik. The carriage runs on a double side rail bearing combination made by Thompson. The scanner top is made of an aluminum honeycomb sandwich panel, called "Hexcel", made by Pacific Panel. The scanner sits on a Unistrut frame.

MINERνA's scanner will not be identical to MINOS' due to the different dimensions of the two detectors' scintillator components. The MINOS scanner covers an area 1.2 m by 10 m. MINERνA's needs to scan an area about 4 m square. By strengthening the carriage, we can extend its range in the short dimension from 1.2 m to 4 m. It may also prove more economical to construct the support frame from welded aluminum rather than Unistrut.

The scanner will employ a 5 mCi Cs-137 source, similar to the type used by MINOS, collimated by a machined lead cone. At least 5 cm of lead on the sides are required for collimation, with at least 2.5 cm of lead on top for shielding. The source will be mechanically connected to the lead cone to prevent removal. Fermilab's Safety Division will review and approve the final design to ensure the shielding is sufficient protect the scanner operators and others from exposure to hazardous levels of radiation.

The signal and readout system for the source scanner will be the MINERνA PMTs, PMT boxes and data-acquisition system.

The modules should be light tight when we scan them, but a tarp will be available to help track

//

Figure 60: The MINOS source scanner. MINERνA will construct a similar device to scan scintillator pans after construction to control quality and map local response.

down and fix light leaks that may have been created during transportation. Once a module is placed on the scanner and its light-tightness is verified, the scan will begin and run automatically overnight. We expect to scan one pan per day. Based on MINOS experience, the scanner can make 4 measurements per minute, including the movement of the source. Thus, we can do about 5000 individual measurements on each module, corresponding to 10 scans along the fiber direction, each scan involving 500 steps perpendicular to the scintillator strips. This will produce enough data to fit each fiber to a double exponential function, and provide a good description of its attenuation.

10.3.5 Detector stand

The detector stand will consist of two rails approximately 20 feet in length. Each rail is supported by four vertical posts of structural steel, with a structural steel bookend at the downstream end. The "keys," which lock the 4-plane module assemblies into the structure, are made of stainless steel (or a combination of stainless and brass) to prevent the supports from becoming magnetized. There will be 100 of these (2 each for 50 modules) and their manufacture will constitute most of the machinist's time for this item. The sum weight of all of the modules is estimated to be 211 tons plus a possible 91 tons for an eventual muon ranger, exclusive of cabling, electronics and other accoutrements. The preliminary design calls for the stand to support 400 tons.

We intend to build two support structures, one shorter structure for module assembly at the suface and one for support below ground in the MINOS near hall. The module assembly and the assembly stand itself would be at New Muon Lab. The underground support structure should also be assembled first on the surface, at the New Muon Lab. The purpose of the above-ground assembly is to test the structure itself and de-bug assembly procedures. It will be modified as necessary, then disassembled and moved underground to the MINOS hall. All critical welds will be made on the surface. Underground assembly will consist of rigging and bolting.

10.3.6 Module installation

The MINERνA installation is expected to proceed much like the MINOS near detector installation: a complete module will be placed on a strongback, driven from New Muon Lab to what is called the "MINOS shaft", then lowered down the shaft onto a cart at the base of the shaft. This cart then transports the module plus its strongback to the MINOS hall, where a second crane will pick up the strongback and module and place both on the detector support stand. Then the module will be connected to either the bookend or an already installed module, the strongback removed from the module, and brought back up to the surface.

This task is assumed to be straightforward, based on experience with the MINOS installation. It is possible that some materials left over from MINOS could be used in the fabrication of the strongback. Also, the cart that was used to transfer MINOS near detector planes while underground might only need some modifications to be used for MINERνA modules.

One attractive possibility is to assemble the modules on the strong back, and the individual pieces would therefore be lifted with slings and placed on the strongback. In this way an additional custom-built lifting fixture other than the strongback itself will not be necessary.

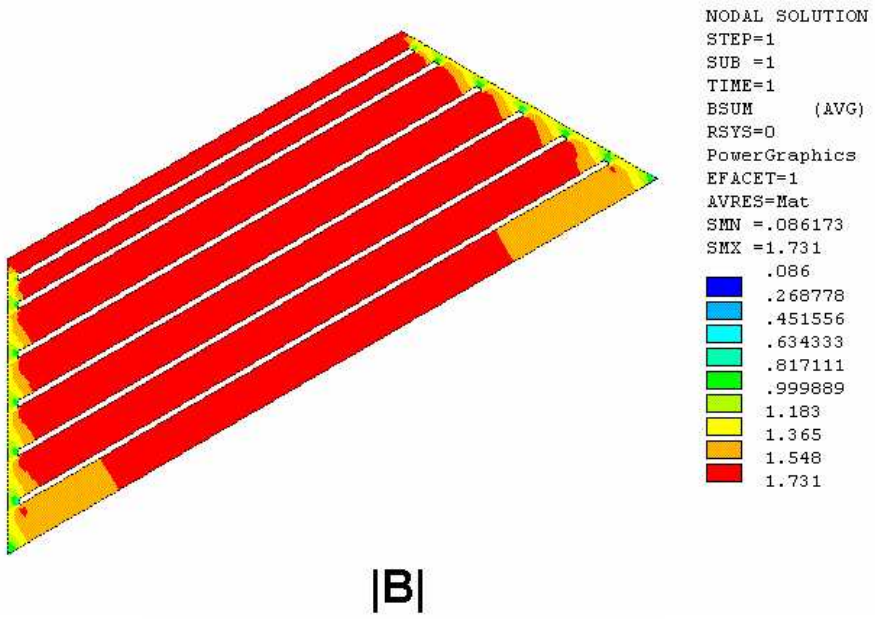

Figure 61: A preliminary calculation of the expected magnetic field ($|B|$ in Tesla) in MINERνA frames made from 1009 steel and energized by a 28,000 A current.

10.4 Magnetic Coil

This section describes the requirements of the MINERνA coil, and what these requirements imply for the coil design. Much of the design of the coil is borrowed from that of the MINOS near detector.

To achieve a high magnetic field and the best possible momentum resolution, the current must be high enough to saturate the low-carbon steel. Finite-element analysis calculations have shown that 28,000 A-turns will suffice, yielding a toroidal magnetic field of 1.6 T for 1009 low-carbon steel. The calculated field is shown in Figure 61 and the field in a radial slice is shown in Figure 62. The effect of the field will be to focus radially escaping negatively-charged tracks (i.e. muons) toward the MINOS near detector.

The coil turns will be installed through the completed detector modules and will be the final piece of heavy installation during detector construction. The space requirements and installation plan lead to a design with a minimum number of turns and high current per turn, as in the MINOS near detector [170]. This high current on the coil turns will require substantial cooling. A low-conductivity water (LCW) closed loop provides the coil-cooling for the conductor.

The coil consists of 11 approximately 5.5 m legs (bore and return) and 12 approximately 1.5 m-long sections to connect the bore and return legs (upstream and downstream).

Each coil leg is formed from 2.8×3.8 cm^2 rectangular cross-section aluminum conductors with a 1.66 cm diameter channels through their centers. The conductor is cooled by flowing LCW through the center channel. The cross-section of the one of these conductors is shown in Figure 63. The coil cross-section has 36 of these conductors.

Groups of six conductors are formed into planks (Figure 64). The electrical connections are made using edge-welded lap joints. An example of one of these joints from MINOS is shown in Figure 65. The current flows in parallel through the conductors within a plank. The lap joints require less installa-

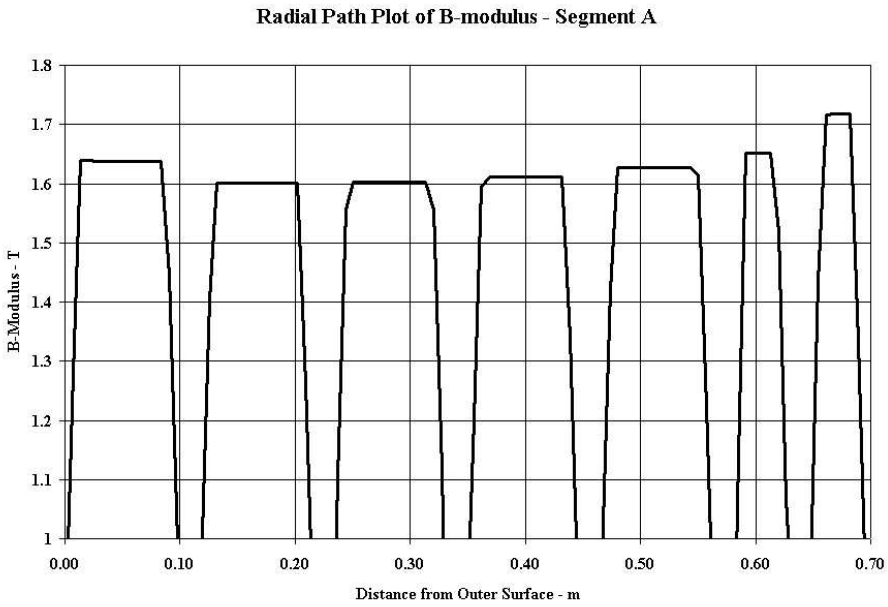

Figure 62: A preliminary calculation of the expected magnetic field ($|B|$ in Tesla) in a radial slice through a MINERνA frame made from 1009 steel and energized by a 28,000 A current.

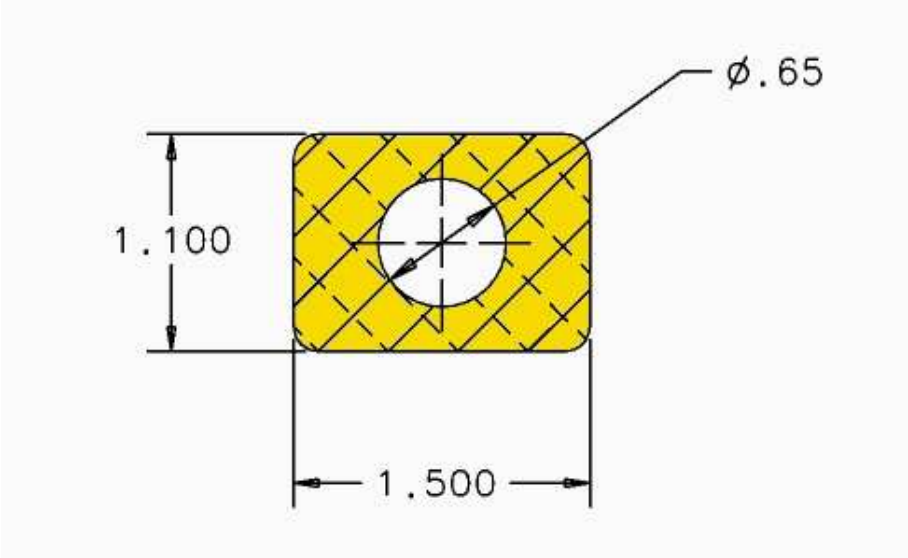

Figure 63: Cross-section of an aluminum conductor element. The dimensions shown are in inches.

Figure 64: Cross-section of a MINOS coil plank. An identical design is proposed for each turn of the MINERνA coil.

tion labor than designs requiring conductor-by-conductor in situ welding.

Input and output water manifolds will be located at all four corners of the device. Water passes through four planks before returning to the chiller, giving six separate parallel water circuits. The water flows in parallel within a plank. Flow calculations show that the flow rates in the different conductors within a plank are fairly well balanced [171].

There is only one electrical circuit. Each conductor carries up to 833 A and the coil is powered by a 5000 A supply.

10.4.1 Manufacture and installation

The pre-tested aluminum conductor is purchased from a vendor and delivered directly to the coil fabricator on spools where it is uncoiled, straightened, and cut to length. The ends of the conductors are prepared for welding in two ways: the hole is countersunk for a stainless-steel ferrule and the edges are beveled to allow for full penetration welds. The six conductors in a plank are welded together. Ferrules are inserted into the lap-joint pieces and mated with the conductors and then welded. The planks are wrapped in two layers of G10 and B-stage epoxy and heat cured. The finished planks are then pressure and flow tested prior to delivery to Fermilab.

After delivery the completed components are lowered into the NuMI near detector hall though the shaft using a special lifting fixture. Because the MINERνA coil will be significantly shorter than the MINOS near detector coil (5.5 m compared to 20 m), the installation will not be nearly as challenging.

The coil will be installed after the detector has been mounted. Planks are rigged into position using a special "spreader bar" lifting fixture to support the free end of the plank as it enters the bore. Note that the center segment of the coil assembly (six full-length planks) weighs about 100 kg. The planks are flexible, and could be easily damaged if overstressed. Before the lap connections are made the surfaces

Figure 65: Completed MINOS planks showing lap joint end pieces.

will be chemically cleaned and a surface coating will be applied. After a new plank is put in place, the lap-joint connection is completed. There is a relatively short time (minutes) between the preparation of the surface and the mating of the splice.

Before the installation can proceed, brackets are mounted on the steel support structure to support the return coil. Installation of the first four planks is somewhat different than the remainder of the planks. Rollers on the lifting fixture enable the planks to slide smoothly into the bore of the detector, where they rest on insulation in the central collar tube. The long return plank is then rigged into position on the support brackets under the detector. A short plank is rigged into position on the downstream end of the detector and connected to the first two planks. Each connection will be checked for electrical integrity. The water connections to each end of the planks will also be made. A second short plank is installed on the upstream side of the detector and is only connected to the return plank. This completes the first circuit of planks. After this point, the installed coil sections are self-supporting.

The remaining planks are installed in a helical pattern. First a bore plank is installed, then a downstream plank, then a return plank, and finally an upstream plane. As each plank is installed it is electrically connected to the previous plank and protective insulation installed. Final installation of the coil includes making connections to the power supply and tests of the LCW system.

10.4.2 Cooling systems

The coil cooling system will connect to the MINOS halls LCW cooling system. The coil cooling system will run at about 70 GPM and must carry off the 25 kW of heat generated by the coil power supply, coil, and power bus. Fermilab will install additional cooling to the detector hall accommodate this load.

10.4.3 Power system

The coil will be powered by a Fermilab PEI 150-5 supply running at 5 kA to deliver up to 5000 A or 833 A per conductor. The power supply has remote readout and remote control capabilities. The supply, cooling system, and interlocks will be provided by the Fermilab.

The supply's control and monitoring systems will be interfaced to the Fermilab ACNET control system in keeping with standard practice for analysis magnets. There will be a parallel read back to the MINERνA slow control systems and parallel read back and control for the magnetic calibration system. As in MINOS, manual connections at the supply will be used to change the control source.

The coil power supply will have a current regulator and precision readout to continuously monitor its current. In addition a resistance bridge will be installed to monitor for small changes in the resistance of the coil that could signal non-uniform heating or shorts. Thermal interlocks will also be provided in the event of excessive heating or loss of LCW flow.

The coil will also have a 5 kA mechanical reversing switch to allow the polarity to be reversed. The switch will have remote control and monitoring capabilities and will be interface to ACNET for control and the MINERνA slow control system for read back.

10.4.4 Magnetic calibration

Calibration of the magnetic field will be done by the installation of induction coils at several radii per plane. These coils will be read-out by a PC with Keithley scanning ADC and I/O board using a LabView program.

Although the coils themselves (called Bdot cables) must be purchased, all other hardware can be recycled from MINOS.

10.5 PMT's, Optical Boxes and Cables

10.5.1 Multi-anode PMT's

With an inexpensive active detector technology, the dominant equipment costs for MINERνA are photosensors and their associated read-out electronics. Our choices among the universe of available technologies is determined by the answers to three questions. First, is the light yield for a minimum-ionizing particle sufficient to support a low quantum-efficiency detector such as photomultiplier tubes (PMTs) or image intensifier tubes (IITs)? In MINERνA, there is sufficient light to use a $1/6$ quantum efficiency photocathode with a WLS fiber diameter of at least 1.2 mm, as explained in Section 11.3. Second, is timing within the spill important or can a technology that integrates over a long window, such as IITs be used? We concluded that timing within the spill, both to flag overlapping events and measure time of flight and decay times at rest was important to our physics goals. Third, what level of technical risk, R&D time and cost is acceptable? We concluded that for MINERνA to begin data-taking as early as possible, and given the modest size of our collaboration and expected detector costs, we should choose low technical risk over lengthy R&D programs designed to reduce costs or improve performance.

In our design process, we considered four technologies for photosensors: multi-anode photomultiplier tubes (MAPMTs), IITs, avalanche photodiodes (APDs) and visible light photon counters (VLPCs). Ultimately, we chose a solution based on MAPMTs with a sensor+electronics cost (including EDIA and overhead but without contingency) of approximately \$40 per channel, approximately divided between

$15 per channel for the sensor, $15 for the electronics and $10 for EDIA and testing. To defend this important decision, we discuss the alternatives mentioned above.

Image intensifying tubes coupled to CCDs are an appealing low-cost solution for reading out bundles of fibers, in part because the CCD itself is the final stage photosensor and readout device. This device is well-matched to the pulsed structure of a neutrino beam, with one readout corresponding to one beam pulse. Costs per channel are largely proportional to the total photocathode surface required, which is set by the number of channels and fiber diameter. Cross-talk in adjacent channels is a non-trivial issue, but can be addressed because of the high density of CCD channels relative to fiber granularity, even with intermediate spatially demagnifying stages. We were driven to relatively expensive CCD cameras because of the need maintain reasonable linearity. Our candidate system, based on Hamamatsu C8600 2-stage multi-channel plate (MCP) intensifiers and C7190 bombardment CCDs, was approximately $15 per channel, including photosensor and CCD readout but not including required demagnification optics. Nevertheless, a complete IIT/CCD system would likely still be half the cost of the chosen MAPMT solution. Our concerns about the system were the smaller effective dynamic range, even with relatively costly IIT/CCD systems, and the relatively low mean time to failure per device reported in other large systems (4 years per two stages in the CHORUS experiment). However, the missing capability for timing within a single main injector spill was enough for us to discard this otherwise promising option.

Avalanche photodiodes (APDs) were also considered because of their recent successful application in the CMS ECAL and their proposed use in the NuMI off-axis far detector. APDs are low gain ($\sim$100), high quantum efficiency (85% for Y11 WLS fibers) devices which offer significant cost savings in the photodetector. Complications of operation include the need to cool the sensors below room temperature to reduce noise, but this is a fairly easily solved problem as cryogenic temperatures are not required. The primary problem we identified with APDs for MINERνA was the need for significant electronics R&D to develop a low-cost system for controlling noise over the long NuMI spill. For MINERνA, we set a requirement of keeping the photosensor and electronics noise well below 10 delivered photon equivalents to maintain good sensitivity to minimum-ionizing particles (typically 70 photons in a doublet of triangular scintillators) and a low rate of detector noise. Over a 12 μs gate (the NuMI spill plus $2\tau_\mu$) at -10°C with an operating gain of 100 (optimal), the signal from 10 photons is 850 electrons and the noise on the best existing candidate electronics, the MASDA chip, is 900 electrons. To achieve the better signal-to-noise being pursued by the proposed NuMI off-axis R&D program requires design of a new ASIC, which would imply at least a one-year development project. In short, although the APD is a potentially promising technology, we were not convinced it could be in production on a timescale suitable for MINERνA.

The final alternative considered was the VLPC. These have a history of successful employment and electronics design in the D0 fiber tracker and pre-shower detectors. However, the costs for just the VLPCs themselves, even under optimistic assumptions about the outcome of future R&D, would exceed $50 per channel, and are thus significantly greater than the MAPMT solution. Given that the low quantum-efficiency solution gives sufficient resolution, it is difficult to justify the cost of VLPCs.

The MAPMT we have selected as our photosensor is the Hamamatsu R7600U-00-M64. These are an incremental design improvement from the R5900-00-M64 MAPMTs used in the MINOS near detector, and we expect much of the experience gained by the MINOS collaboration with these detectors to be applicable. In particular, we have confidence in costing the testing, housing for and optical connectors to the PMTs because of our ability to scale costs from the MINOS experience.

10.5.2 PMT testing

James Madison University (JMU) will build a test stand for evaluation of MINERνA's Hamamatsu M64 photomultiplier tubes (PMTs). The M64 PMT is currently used by MINOS, and the results of their tests have been submitted for publication [167]. Each MINERνA PMT will undergo a similar series of tests to verify its suitability for use in the experiment. Tubes passing specified acceptance criteria will then have their performance characterized in detail.

The JMU test stand is designed to test 5 M64 PMTs simultaneously, with an additional witness PMT for reference. The pixels of the M64 are arrayed in an 8×8 lattice. Bundles of 64 clear optical fibers will be connected to the pixel arrays of the six PMTs in the test stand. A wavelength-shifting (WLS) fiber bundle mounted on a computer-driven stepper motor table will allow illumination of any of the clear fiber bundles. The light intensity may be varied with a neutral density filter wheel between the clear and WLS fibers. A pulser-driven blue LED will serve as the light source for the test. Figure 66 shows a schematic of the test set-up.

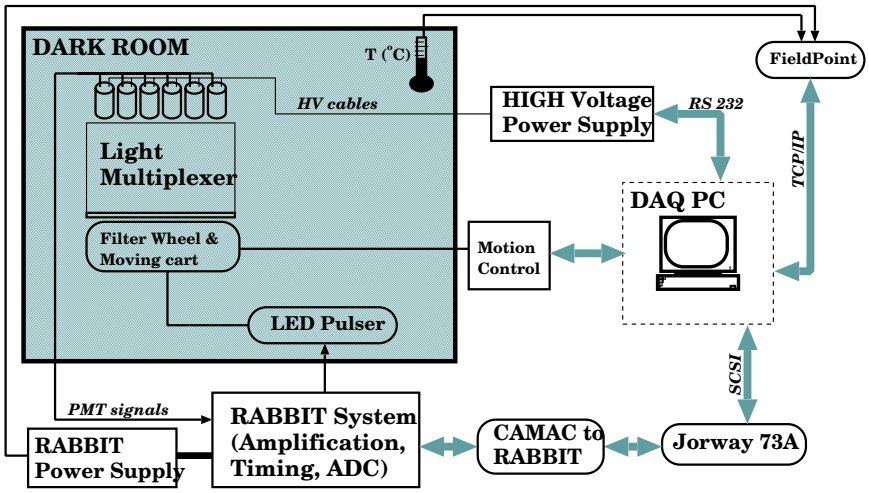

Figure 66: Schematic of the University of Athens MINOS PMT test stand and associated electronics which serves as a prototype for the JMU test stand to be constructed for this project. Note that we plan to replace the RABBIT system shown in this diagram with MINERνA electronics for the final test stand.

Each PMT will undergo a series of tests to qualify it for service in MINERνA and record the relative response of each pixel.

- Gain vs. voltage in the range 500–1000 V will be measured at a light level of 10–15 photoelectron using a stable pulsed LED source.

- Width of the single photoelectron peak will be measured using the same LED pulser with 0–1 photoelectrons per pulse.

- Linearity of charge response. Space charge effects in MAPMTs can be a problem due to the small size of the dynodes, and MINERνA relies on measurements of high dE/dx for proton

identification and electromagnetic shower energy reconstruction. The filter wheel will be used to map the signal vs. light input relative to a low light standard.

- Quantum efficiencies will be measured by comparing light yields to those of the witness PMT which will, in turn, be calibrated against a Hamamatsu supplied standard.
- Dark current at operating voltage within a MINERνA ADC gate. A high number of pulses will be measured with the MINERνA gate to ensure that few of these gates are populated above a 1/3 photoelectron threshold from dark current.
- Inter-pixel cross-talk will be measured by illuminating single pixels over a variety of light levels and observing their nominally dark neighbors.

These tests will require an estimated 3 days for one batch of PMTs. For each test, 5000-10,000 pulses per pixel per setting will be acquired. For example, to test linearity we plan to acquire 5000 events per pixel using 12 different filter densities. The total number of pulses would be $64 \times 5000 \times 12 = 3.84 \times 10^6$. Assuming a data acquisition rate of 200 events/s this will result in 5.3 DAQ hours. Additional time would be required to move the light source in between measurements. Testing one third of MINERνA's MAPMTs will therefore take about 100 days.

JMU will plan for the capacity to test two thirds of the PMTs needed for MINERνA. Collaborators at the University of Athens, not supported by this proposal, will develop a parallel test stand to test the balance of the PMTs for the experiment.

10.5.3 PMT optical boxes

Design, fabrication, and testing of an operational array of 550 photo-multiplier tube (PMT) optical boxes is one of the critical tasks required in construction of MINERνA [168]. Realization of this array and its delivery to the surface staging area at Fermilab is the primary responsibility of the Tufts and Rutgers groups. Design and prototyping work for a MINERνA-specific PMT box is summarized below. MINERνA boxes, in contrast to optical boxes developed for the MINOS far detector ("MUX" boxes), will house a single M64 phototube per box. Unlike either the MINOS MUX boxes or "Alner boxes" of the near detector, the MINERνA design will use construction-standard steel extrusions reduce fabrication costs and improve magnetic shielding.

Based upon our current design and Tufts' invaluable 2001–2003 experience with production and testing of MINOS MUX boxes, a realistic projection of the costs and schedule has been assembled. Our construction model assumes two coordinated, independently operating assembly and testing sites, one at Tufts and the other at Rutgers. Our breakout of costs and schedules for instrumentation and startup of the factory lines, staffing, purchase and fabrication of component parts, quality assurance testing, and shipping, are detailed in Chapter 12.

PMT box overview In MINERνA, each PMT will reside in a single light-tight box to which optical cables carry the scintillation light from the detector's active regions. Within each box, the enclosed PMT will be in optical contact with polished ends of the bundled fibers which it reads out. This contact is made possible via termination of the fiber bundle in a "cookie" which holds the polished fiber ends. Registration of the fiber-loaded cookie to the PMT is mechanically precise by necessity; it is made possible by a rigid mounting framework which holds the PMT and cookie, whose relative positions are fixed via alignment pins. The fiber mounting cookie is a precisely-machined piece made of Noryll

plastic. In addition to the optical input cable, each PMT box has two electrical cables connected to its associated front-end board: one from a nearby low-voltage power fan-out (Section 10.7), and another for communication with the data-acquisition and slow-control system, which runs in a daisy-chain among twelve boxes (Section 10.6.3). Electrical and optical connections to the interior of each box will be made via endcap connector ports.

To minimize the length of clear fiber cables from the wavelength-shifting fibers to the PMT boxes, we will mount the PMT boxes on the upper surface of the detector itself, using mounting frames of aluminum and steel to provide an air-gap standoff between the optical boxes and the magnetized steel of the outer detector. Since an ambient magnetic field of several tens of Gauss will be present, which could degrade phototube performance, MINERνA optical boxes must provide magnetic shielding for the PMTs, as well as a light-tight enclosure. Specifically, the optical box must ensure that the internal ambient field is below 5 Gauss. Two features of the MINERνA design achieve this goal. First, the box walls will be 1/8-inch steel (3.17 mm), more than twice as thick as either of the MINOS models. Second, the MINERνA design is augmented by mu-metal foil surrounding the PMT, which further deflects the remnant magnetic field.

MINERνA's boxes must be mechanically rugged, protecting both the PMT and delicate fiber hook-up from accidental impacts. The boxes should also be amenable to rapid assembly and testing, and easily disassembled for component repair and replacement. With the latter in mind, we will mount the 64-channel front-end readout board outside each box, enclosed in a pre-shaped aluminum RF shield coverplate. Thus, maintenance of the read-out electronics and Cockroft-Walton HV supply will not require breaking the box's optical seal, or manipulating its optical cables.

The MINOS "Alner" box Successful operation of the MINOS far detector and CalDet hadronic calibration detector testifies to the general viability of the experiment's PMT optical box designs. Of the two MINOS box types, the "Alner" box used in CalDet and the near detector is a PMT-per-box implementation more closely aligned with MINERνA's requirements. Since the Alner box provides a natural starting point for a MINERνA-specific implementation, we briefly summarize its design.

Figures 67, 68 and 69 show front, back, and side exploded-view photographs of an Alner box. An attractive feature is apparent in Figures 67 and 68. The metallic box enclosure is a shell from which the innards are separated; the latter are mounted on a rigid structural frame which is inserted along the axis of the rectangular enclosure. This arrangement has obvious advantages for assembly and alignment of the fiber bundle, fiber cookie, and PMT, providing ready access to these pieces as shown in Figure 69. We have adopted the same strategy in our MINERνA implementation.

MINERνA optical box design The Alner box enclosure (to the left in Figures 67 and 68) is made from thin-wall flat plate which is creased and welded into the finished shape. An equivalent structure is obtainable more economically with construction-standard hollow steel extrusions of rectangular cross section. These can be capped at each end using steel "lids" which are stepped around the circumference. In this MINERνA design, the internal support frame is mounted between these lids; the lids will also carry all of the connector ports. The front lid is smaller than the rear one, allowing axial insertion (as in the Alner box). Standard steel extrusions provide - at lower cost - walls more than double the thickness of Alner boxes, and a modest improvement in magnetic shielding. The original Alner design provided for internal thin-steel magnetic shielding surrounding the PMT, but this was later deemed unnecessary. In our implementation however, interior magnetic shielding is a necessity. A relatively

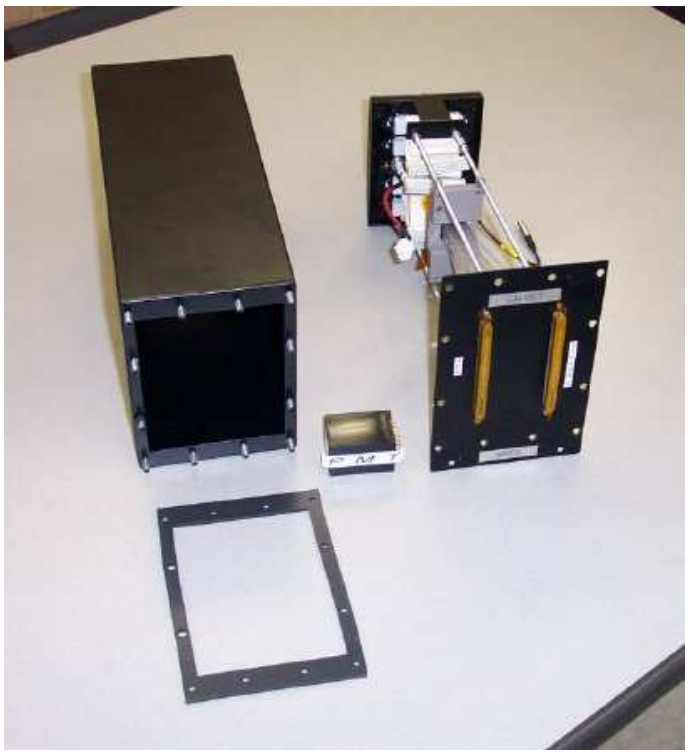

Figure 67: Front view of an “Alner box”, the PMT optical box used for signal readout in the MINOS CalDet and near detector.

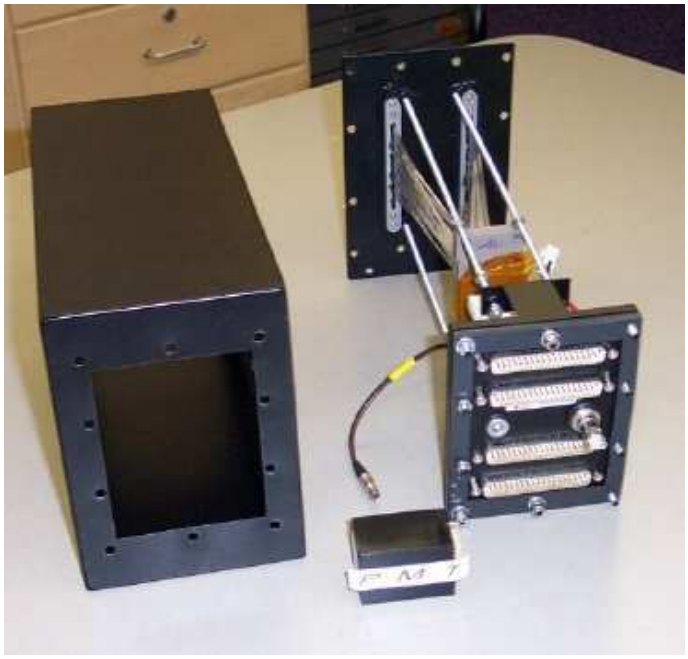

Figure 68: Rear view of a MINOS "Alner box". The framework which holds the fiber cookie and PMT is inserted axially into the surrounding steel enclosure. A similar scheme is used in the MINERνA design.

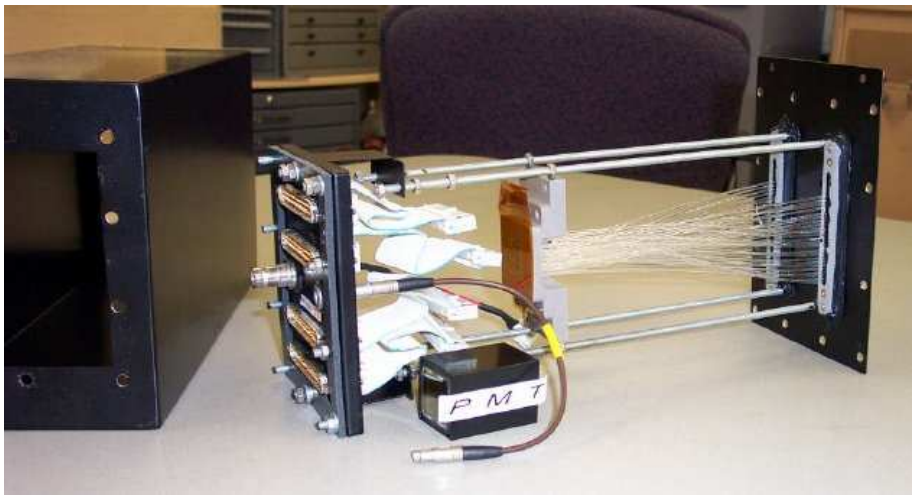

Figure 69: Interior of an Alner optical box. Optical fibers enter via connectors through the backplate and terminate on the cookie. The M64 phototube (foreground) is mounted on registration pins in front of the cookie. Cables provide low voltage and signal connections to the PMT from connectors which breach the front plate.

tight internal shielding surface is achievable using commercially available mu-metal foil; pre-shaped mu-metal forms are also under study.

10.5.4 Fiber connectors and optical cables

MINERνA will use optical connectors from Fujikura/DDK (generically referred to as DDK connectors). These connectors were originally developed for the CDF Plug Upgrade by DDK, in consultation with Tsukuba University. Since then, they have been used by several other experiments (FOCUS, STAR, and D0).

The DDK connectors consist of a ferrule, clip, and box (Figure 70). They snap together without screws and pins. DDK will make a new ferrule die/design for our 1.2 mm diameter fibers, keeping the outside dimensions of the ferrule identical to the current model; thus, other parts of the connector do not need to be redesigned.

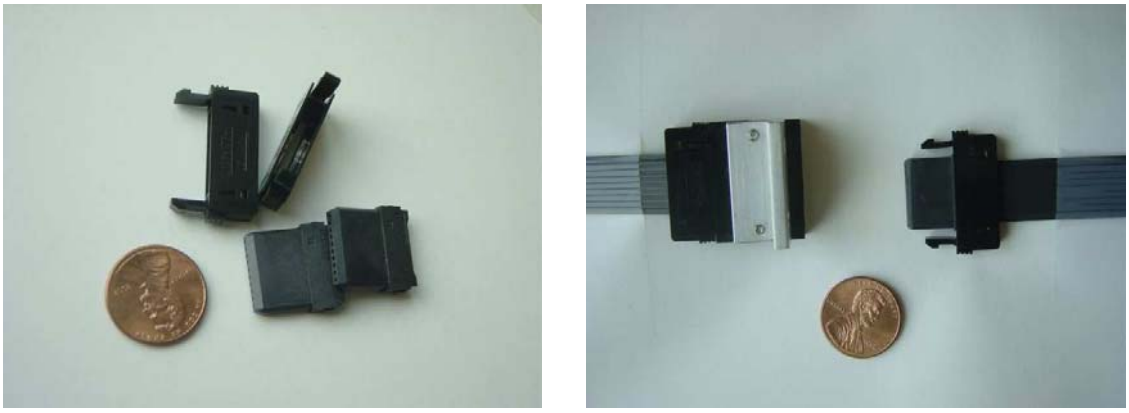

Figure 70: DDK connector parts. At left, examples of the ferrules (bottom) and the clip (top). At right, two completed CDF cables with the box to which they connect. The aluminum angle bolted onto the box is used to hold the box on an aluminum cover.

After mechanically measuring the connectors and performing quality control tests on the fiber, we will assemble wavelength-shifting (WLS) fiber pigtails[5], clear fiber cables, and clear fiber pigtails (the other end of these fibers will be inserted into the acrylic "cookie" for connection to a PMT, see Section 10.5.3).

A sample of fibers from each batch will have their attenuation length checked using a procedure developed by CMS. Fibers will be checked for breaks or cracks during and at the end of assembly. The quality of light transmission for each fiber will be checked once the connectors are mounted.

Our fabrication and polishing procedure was used by the CDF and CMS collaborations on DDK connectors and cables. For the CDF Plug Upgrade, a significant Fermilab effort was devoted to developing a method to polish the DDK connectors. A procedure for polishing one connector at a time is described in [161]; since then, Fermilab has developed a machine we can use to polish 10 optical connectors simultaneously. Fermilab will design a fixture for this machine to hold the DDK connectors.

[5] A "pigtail" is a fiber bundle with a DDK connector on one end; a "cable" is a fiber bundle with connectors on both ends.

Figure 71: The MSU light-tight boot for DDK connectors.

We will use a light-tightening scheme similar to one developed by the Michigan State University nuclear physics group, who used DDK connectors in a large electromagnetic calorimeter. The bulk of the cable is light-tight thanks to an opaque sheath placed around the fiber between the two ends. The region at the connector is made light-tight by placing an RTV (room temperature vulcanizing) silicone rubber boot around the end of the sheath and connector, as shown in Figure 71.

10.6 Electronics

10.6.1 Electronics overview

The requirements for the MINERνA electronics are summarized in Table 9. These requirements are motivated by the experiment's physics goals, which include:

- Fine-grained spatial resolution, exploiting charge-sharing between neighboring scintillator strips,
- Identification of $\pi^{\pm}$, $K^{\pm}$ and p using dE/dx information,
- Efficient pattern-recognition, using timing to identify track direction and separate interactions occuring during a single spill,
- Ability to identify strange particles, and muon decay, using delayed coincidence, and
- Negligible deadtime within a spill.

The average data rate expected for MINERνA ($\sim$ 100 kByte/second) and the relatively modest duty-factor of the NuMI beam (one $\sim$ 10 μs spill every 2 seconds) are far from demanding by the standards

of modern high-energy physics experiments. To minimize costs and technical risks, we have studied a number of existing solutions, including those used for the MINOS design. Major components of the electronics system include the front-end boards, the PMT and electronics housing, slow control and readout systems. Extensive prototyping and integration testing will be performed for all components prior to production of the final modules.

10.6.2 Front-end electronics

The front-end boards digitize timing and pulse-height signals, provide high-voltage for the photo-multiplier tubes (PMTs), and communicate with VME-resident readout controller modules over an LVDS token-ring. For easy access in connection, testing and replacement, the boards are mounted *outside* the light-tight PMT housing assemblies. Pulse-heights and latched times will be read from all channels at the end of each spill.

The front-end board for MINERνA is designed around the D0 TRiP ASIC which is a redesign of the readout ASIC for the D0 fiber tracker and preshower. As discussed below, the TRiP chip has suitable capabilities for use in MINERνA. The most significant technical risks have already been addressed by our successful 2004 R&D program, using a prototype board fabricated using available TRiP chips from D0. Results from the prototype board are discussed in detail in the R&D section of the MINERνA Technical Design Report.

Requirements and design features Each front-end board will service one PMT (64 channels) which will require 4 TRiP chips per board. The TRiP chips will be controlled by a commercial FPGA (Field-Programmable Gate Array) using custom firmware. A prototype of this firmware has already been developed and successfully operated during our R&D studies. In addition to digitization of charge and timing information, the front-end boards will also supply high-voltage to the PMT and communicate with the downstream readout system over an LVDS (Low-Voltage Differential Signaling) link. Figure 72 shows the basic design of the board and the main components. Table 10 summarizes the channel counts for the final design.

Parameter	Value	Comments
Active spill width	12 μsec	Spill plus $2 \times \tau_\mu$
Repetition Time	$>$ 1.9 sec	
Number of channels	37478	
Occupancy per spill	2%	LE beam, 2.5×10^{13} POT/spill
Front-end noise RMS	$<$ 1 PE	
Photodetector gain variation	4.5 dB	Extremes of pixel-to-pixel variation
Minimum saturation	500 PE	Proton range-out or DIS event
Maximum guaranteed charge/PE	50 fC	Lowest possible charge at highest gain
Time resolution	3 ns	Identify backwards tracks by TOF
		Identify decay-at-rest $K^\pm$, $\mu^\pm$

Table 9: Electronics design requirements and parameters for MINERνA

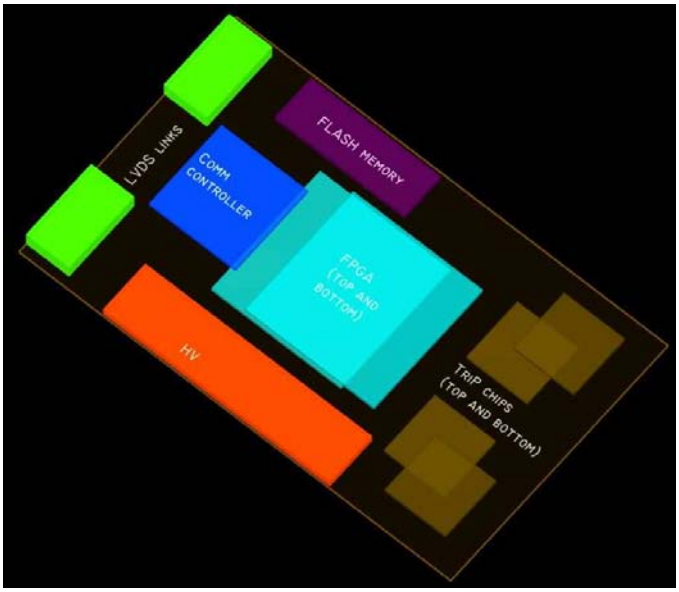

Figure 72: Simplified schematic of the front end electronics final board.

Item	**Quantity**
Front-end boards, including spares(15%)	580
PMT's serviced per board	1
PMT channels serviced per board	64
ADC channels per board	128 (64 low-gain and 64 high-gain)
TDC channels per board	64
TRiP chips per board	4
LVDS interfaces per board	2 (1 send + 1 receive)
HV channels per board	1
Power consumption per board (including PMT HV)	7 Watts

Table 10: MINERνA front-end board channel summary.

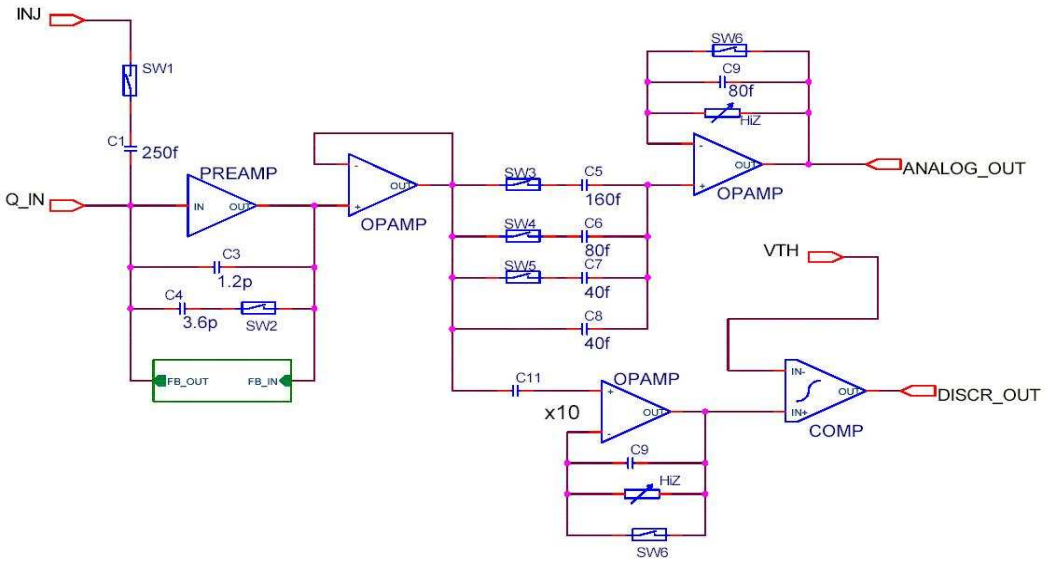

Figure 73: Simplified schematic of the front end electronics of the TRiP chip.

The TRiP chip and digitization The heart of the system is the D0 TRiP ASIC. The TRiP chip was designed by Abder Mekkaoui of the Fermilab ASIC group and has undergone extensive testing by D0 [169]. Its analog readout is based on the SVX4 chip design. Each TRiP chip supports 32 channels for digitization, but only half that number of channels for discrimination and timing. A simplified schematic of the TRiP ASIC is shown in Figure 73. The pre-amplifier gain is controlled by jumper SW2 and has two settings which differ by a factor of four. The gain of the second amplifier stage is controlled by jumpers SW3-SW5. We will set the chip to the lowest gain setting for the preamp and largest integration capacitor. This gives a linear range with a maximum charge readout of 5 pC. The "ANALOG_OUT" goes into a analog pipeline, which is identical to the one used on the SVX4 chip and 48 cells deep. To gain dynamic range, MINERνA will increase the input range of the electronics by using a passive divider to divide charge from a single PMT anode among two TRiP channels with a ratio of a factor of 10. This "high range" channel, then, will give a equivalent total readout charge of 50 pC. Each TRiP channel will be digitized by a 12-bit ADC.

Based on Monte Carlo studies of proton identification by dE/dx, the MINERνA design requires no saturation below 500 photoelectrons (PE) and RMS noise well below 1 PE. Matching this to the 5 pC charge limit, the highest gain anodes in a tube would be set at 100 fC/PE and therefore the lowest gain anodes would be run at 33 fC/PE. In MINERνA the integration time for the ADC will be 10–12 μs, much less than the hold time for the charge in the capacitor of 100 μs. The prototype MINERνA board has been tested explicitly with a 10 μs gate, and the measured pedestal RMS was < 2 fC. This will put a single photoelectron approximately a factor of 10 above the pedestal RMS, well within our requirements. The maximum PMT gain for the lowest gain anode will be 50 fC/PE, safely within the desired parameters above.

Timing Only one of every two input channels to the TRiP chip has a latched discriminator output (latch) which can be used for timing information. Hence, only the lower range channels will feed the

latch whose output will then go into an FPGA. With appropriate firmware, internal logic of the FPGA can be used measure timing with a granularity of 5 ns. To measure the time of the latch firing accurately, the RF/2 reference clock from the Tevatron (approximately 25 Mhz) is multiplied by four in a PLL and phase shifted by 90 deg to form a quadrature clock that is used inside the FPGA to form a digital TDC with least bit resolution of 2.5 ns. This feature has also been tested on the prototype board and a timing resolution consistent with the 2.5 ns least count timing resolution of the TDC's has been achieved. The reset time for the latch is only 15 ns, so inside a spill the latch will be in the ready state by default. When the signal exceeds a threshold of 1.5 PE, the latch will fire. After storing the time, the latch is reset, incurring minimal deadtime.

Each board includes its own high-frequency phase-locked oscillator, which provides a local clock signal for the FPGA logic. Global synchronization is provided using an external counter-reset reference signal distributed over the LVDS interface from the VME readout boards once every second, and originating with a MINOS timing module which is, in turn, synchronized to the NuMI beam.

High-voltage A resonant mode Cockroft-Walton high-voltage generator, mounted on a daughter card, will provide power to each board's PMT. The daughter-card design will allow a malfunctioning high-voltage supply to be easily replaced without changing the main readout board. A controller based on the Fermilab RMCC chip, very similar to one already being developed for the BTeV experiment, will allow the PMT voltage to be monitored, adjusted or disabled under computer control, using the LVDS interface to the board.

LVDS interface As detailed in Section 10.6.3 each front-end board will be a member of a chain (or token-ring) connected by LVDS to a VME-resident readout controller. As such, the front-end boards require two LVDS connections, one to receive data from the previous member, and another to transmit data to the next. The LVDS interface transmits all information to and from the board (at 53 MHz), including:

- Transmission of digitized timing and charge data from the front-end board to the VME readout controller,
- Write access to the front-end memory buffers, for diagnostics,
- Configuration of the TRiP chip registers (thresholds, gains, etc) for data-taking,
- Reprogramming of the flash ROM containing the front-end board's FPGA firmware, and
- High-voltage control and monitoring messages.

The first prototype front-end board used in our 2004 R&D studies was designed to accommodate an LVDS interface, which will be commissioned and tested in early-2005.[6] This subsystem represents the most significant remaining technical risk in the electronics (now that the TRiP digitization and timing scheme has been successfully tested), as the latency in propagating signals from one front-end board to another via LVDS limits the number of boards that may be linked in a single chain, and hence the number of chains (and VME readout boards) required to service the full detector. The latency tolerance

[6]For testing and commissioning the board's core digitization functionality, an alternative parallel-port interface was used during initial R&D studies.

is constrained by the need to transmit a global timing synchronization signal to all front-end readout boards. As explained in Section 10.6.3, pending prototype testing we estimate approximately 100 ps jitter may be introduced by each link in the chain. As the least count of our TDCs is 2.5 ns (which is itself considerably better than required, since each track will have numerous timing measurements) we have conservatively limited the design length of each LVDS chain to 12 boards, which represents a factor of two safety margin ($12 \times 100\,\text{ps} = 1.2\,\text{ns}$) from a single TDC count. As LVDS is a mature technology, used in many consumer applications, this risk is a relatively mild one, which in the worst case would require fabrication of a small number of additional VME readout boards and/or a modest compromise in timing resolution which will not noticeably degrade the experiment's physics capabilities. Based on results from the first prototype, the final version of the LVDS interface will be designed and incorporated into the second (64-channel) prototype, and the full token-ring communication protocol defined, for testing together with a prototype of the VME readout controller.

FPGA and firmware The internal behavior of the front-end board is supervised by an FPGA operating as a finite-state machine, making the system programmable and highly flexible. As noted, during commissioning of the first prototype version of the board during 2004 R&D, the most mission-critical and timing-sensitive elements of the firmware (controlling the TRiP chip's buffering and TDC functionality) have already been developed and successfully tested. For the production boards, logic to interpret commands and exchange data over the LVDS interface, and control the on-board Cockroft-Walton high-voltage supply will also be required. This additional logic can be developed and tested using the full 64-channel prototype version to be built during 2005.

Persistent storage for the firmware is provided by an onboard flash PROM, which is read by the FPGA on power-up and can be re-written under computer control. As such, it will be possible to reprogram the FPGA logic of all boards remotely even after they are installed, if necessary.

10.6.3 Data acquisition and slow control

MINERνA's data acquisition (DAQ) requirements are relatively modest, as the average data rate expected in the NuMI beam is only 100 kByte/second and a two-second window for readout is available after each $\sim$ 10 μs spill. Moreover, the predictable timing of the beam obviates the need for a complicated trigger - instead, a gate is opened just prior to arrival of the beam, and all charge and timing information from the entire detector is simply read-out after the spill is complete. The slow-control system is also relatively simple, with each PMT powered by its own local Cockroft-Walton HV supply (resident on its associated front-end board).

The DAQ and slow-control system is therefore essentially a communication network for distributing information (synchronization, high-voltage commands, and exceptionally, updated firmware) to the front-end boards and funnelling event data collected from them to the main data acquisition computer. The system consists of the following components:

- The main DAQ computer, including a VME interface board,
- Two VME crates containing a total of 11 custom-built Chain Read-Out Controller (CROC) modules, with each CROC controlling four LVDS chains,
- 42 LVDS chains (CAT-5e network cable), with each chain linking 12 front-end boards, and
- A third VME crate, containing timing, diagnostic and logic modules.

Due to the distributed nature of the front-end digitizer/high-voltage boards, the central DAQ and slow-control system itself can be easily accommodated in a single electronics rack.

LVDS token-ring chains As explained in Section 10.6.2, the front-end digitizer boards are daisy-chained into 42 LVDS token rings of 12 boards each. Data is transfered over the LVDS at 53 MHz, a frequency much higher than required for data readout, but necessary to transmit precision synchronization reset signals to the front-end digitizer boards. Both ends of a chain terminate in a custom built VME chain read out controller (CROC) module described below. The number of digitizers on a chain is limited by the allowable jitter in the high-precision timing information transmitted to each digitizer board over LVDS. As LVDS is a one-way protocol, each digitizer board must receive the period global synchronization signal from the previous member of the chain on one connection, and re-transmit it to the next member on a second connection. Pending bench tests with our 16-channel prototype front-end board, to be completed by early 2005, we estimate that each board in a chain will introduce approximately 100 ps of jitter; thus a chain consisting of 12 boards would translate into roughly 1.25 ns timing jitter (worst case). This represents a factor of two safety margin over the 2.5 ns least-count timing resolution of the front-end TDC's. In the unlikely event the jitter introduced by a chain of 12 front-end boards proves unacceptable, even with this large safety factor, the number CROC modules (and hence chains) could be increased, allowing each chain to have fewer members.

LVDS signals will be transmitted around a ring on standard, commercially-available fire-resistant and halogen-free CAT-5e network cable approved by Fermilab safety division for underground use. The LVDS chains will also be used to transmit configuration and slow-control messages to the cards.

Chain read-out controller (CROC) modules Each CROC module will control four LVDS chains, requiring a total of 11 CROCs (plus spares) for the entire detector. These modules will reside in two VME crates alongside a crate controller and a MINOS timing distribution module.

The readout controller modules have the following functions:

1. Prior to the arrival of a NuMI spill, as signaled by the VME-resident MINOS timing module,[152] to reset the timing counters of each front-end board and open a 10μsec gate to collect data from the spill.

2. Upon completion of a NuMI spill, to initiate readout of front-end digitizer data over the four associated LVDS rings, into internal RAM.

3. Upon completion of the parallel readout of all four chains, to raise an interrupt with the main DAQ computer, indicating that event data is available. The PVIC/VME interface/crate controller allows VME interrupts to be received directly by the main computer.

4. The internal RAM of each CROC is memory-mapped to the host computer's PCI bus, allowing block transfer of event data via the PVIC/VME interface/crate controller. The relatively long NuMI duty cycle ($\sim$2 seconds) and low data rate (under 1MB per spill for the entire detector) ensures that no deadtime will be associated with the readout itself.

5. Once per second, to globally synchronize the detector's TDCs over LVDS using a high-precision refresh signal from the MINOS timing module. The need for this synchronization drives the choice of LVDS for the readout chains, as opposed a lower performance alternative such as Ethernet.

6. Upon command of the main data acquisition computer, to control and monitor the Cockroft-Walton high-voltage power-supplies on the front-end digitizer boards, and to configure the firmware of these boards at run-startup.

Ancillary electronics and DAQ computer Communication between the main data acquisition computer will be via commercially available PVIC/VME link, allowing block data transfers to and from VME and interrupts to be received by the computer in response to the NuMI spill gate.

A trigger scaler and TDC to monitor the NuMI timing signals, and a programmable pulse generator to simulate them during beam-off periods, along with other any additional logic needed for monitoring and calibration, will reside in the third VME crate. All VME components will be installed underground, within about 20 meters of the detector.

The main DAQ and slow-control computer will be located near the VME electronics, in the NuMI hall, with two high-speed TCP/IP links (one for data, one for monitoring and control messages) to the Fermilab network. A relatively modest, dual-CPU server model will be more than adequate for our purposes. One CPU will be dedicated to real-time data acquisition, and the other will handle control messages and monitoring. An on-board, RAID-5 disk cluster with sufficient capacity to store several weeks of data will serve as a buffer for the data, pending transfer to offline processing nodes and permanent storage.

Component	Number	Comments
Channels	30992	WLS Fibers
Front-end boards	503	One per PMT, plus 15% spare
Readout Token Rings	42	12 PMTs/ring
VME Readout Cards	11	4 rings/card, plus five spare
VME Crates	3	Plus one spare
VME PVIC Interface	3	One per crate, plus one spare
PVIC/PCI Interface	1	Plus one spare
DAQ Computer with RAID system	1	Data rate is 120 kByte/spill

Table 11: Parts count for MINERνA electronics design

10.7 Power and Safety Systems

10.7.1 Quiet power

The current design calls for a complement of electronics and DAQ components that will not quite fill one electronics rack. The sum power draw of these items is estimated to be 3 kW.

Also in the rack will be a Fermilab-provided low-voltage power supply for the front-end boards mounted in the individual PMT boxes. The power required per PMT box will be approximately 7 W, requiring a total capacity of 5 kW. Total Quiet power required for read-out electronics, DAQ computer, front-end electronics and the PMTs is therefore about 8 kW.

To accomodate this, and any other currently unforeseen quiet power needs, Fermilab has agreed to add another 75 kVA transformer to the two 75kVA and one 45kVA transformers already serving MINOS. Like the three existing transformers, MINERνA's would be fed from the main 750 kVA quiet

power transformer, at 480 V. Unused taps with sufficient current capacity exist on this line. Fermilab will also supply electrician labor to install the transformer, conduits, and panel boards.

10.7.2 Magnet power supply

MINERνA will use 48 turns at 500 amps (24 kA-turns) to power the magnetic component of the detector. A 240 kW PEI power supply will likely be used for the MINERνA magnet, and would need to supply 500 A at an estimated 60 V. Unused PEI 240 supplies are available at Fermilab, and will be refurbished at Fermilab expense.

The MINOS magnet will draw an estimated 80 kW on a power supply fed by a 400 A/480 V transformer. Accounting for efficiencies of the supplies, the MINOS and MINERνA magnet power supplies combined should draw less than 200 kVA (236A) from the 400 A/480 V transformer. Fermilab will add a seperate disconnect for the new power supply.

10.7.3 Power distribution

As described above, the MINERνA PMT boxes will each require 48 V volts, and will consume approximately 7 W of power. Analytic Systems has a rack-mounted, 1 kW 48 V power supply which could then supply power for 100 PMT's (model number PWS1000R-110-48). We would use 6 of these supplies, located at the electronics racks. Due to space constraints the racks will likely be many meters from the detector itself. Long cables will go from the six power supplies to fanouts located much closer to the detector, and then shorter cables will go from each fanout to the different PMT boxes located on the detector.

10.7.4 Safety considerations

There are a number of hazards that are associated with the installation and operation of the MINERνA detector: there are mechanical hazards due to the underground nature of the installation and the transport of equipment weighing several tons. There are electrical hazards associated with not only the operation of the electronics, but also hazards associated with the operation of the coil to provide the magnetic field. Finally, there are additional hazards due to the fact that the experiment is to be installed and operated in a deep underground location which has occasional moisture coming from the ceiling. Each of these hazards will be addressed and mitigated in accordance with OSHA, (Occupational Safety and Health Administration) and NFPA (National Fire Protection Association) regulations, as well as the guidelines documented by FESHM (Fermilab Environmental Safety and Health Manual).

The detector stand, the bookends that keep the detector planes straight, and all lifting fixtures associated with transporting the various kinds of detector planes will be designed by Fermilab engineers and reviewed and tested accordingly before they are used underground. Although the coil itself might be fabricated by an outside contractor, the design of the coil will also proceed through Fermilab engineers.

The overall philosophy for MINERνA data-taking is to be parasitic to MINOS data-taking, and the appropriate safety features will be implemented in the detector design to ensure that this is true from a safety standpoint as well.

For example, the MINERνA coil power supply will be adequately shielded to ensure that a separate Lock-out Tag-out (LOTO) procedure will not be required to access the Near Detector Hall while the MINERνA magnet coil is energized. There will also be adequate drip protection above both the

MINERνA detector and coil power supply, since the drip ceiling that covers the MINOS Near Detector does not extend past the MINOS detector itself.

Safety features will also be installed on the MINERνA electronics racks that are similar to those on the MINOS near detector racks. Specifically, the electronics racks will have smoke detection, water drip sensors, air flow, temperature, and humidity sensors.

All the cables that extend to and from the electronics racks, including those that reach the fanouts and from the fanouts themselves to the PMT boxes on the detector proper will be fire-retardant and will be suitable for use underground as defined by Fermilab ES& H section. .

Once the detector, power distribution, and PMT box design is finalized then the current amount of fire protection that is located in the Near Detector Hall will be evaluated to see if additional protection (beyond what is located in the electronics racks) is needed.

11 Detector Simulation and Performance

This section outlines the event simulation and reconstruction software used to optimize the detector's design and quantify its physics capabilities, and R&D studies carried out to validate many key elements.

Much of the simulation software has been borrowed from other experiments, where it has been thoroughly validated. The detector simulation and reconstruction software has been developed specifically for MINERνA, but is based on widely-used libraries and algorithms. MINERνA-specific hardware tests, culminating in a small vertical slice of the detector, to record data from cosmic-ray muons, were carried out over the summer of 2004.

11.1 Event Generators

The MINERνA simulation software interfaces with two event generators that model neutrino interactions with matter: NEUGEN[114] and NUANCE[33]. NEUGEN was originally designed for the Soudan 2 experiment and is now the primary neutrino generator for the MINOS experiment. NUANCE was developed for the IMB experiment and is currently used by the Super-Kamiokande, K2K, MiniBooNE and SNO collaborations. Both have evolved from "proprietary" programs designed for atmospheric neutrino studies into freely-available, general-purpose utilities that aim to model neutrino scattering over a wide range of energies and for different nuclear targets. Total charged-current cross-sections calculated by NUANCE (Figure 75) and NEUGEN (Figure 74) are compared with data below. As the results of the two generators agree with each other (to within the depressingly large range of uncertainties in available data)[117], they have been used interchangeably for the present studies.

As in the past, future studies of neutrino oscillation and searches for nucleon decay will rely heavily on the best possible description of neutrino interactions with matter. Neutrino event generators are tools which encapsulate our understanding of this physics in an easily usable and portable form. Practically, they serve two related functions: to allow the rates of different reactions with the experimental target to be calculated, by providing total exclusive and inclusive cross-sections, and to simulate the dynamics of individual scattering events, by sampling the differential cross-sections. Many comparable packages are available to the collider physics community, and have been incrementally improved for decades, forming a common basis for discussion of different models and phenomena. One important goal of MINERνA is to improve the quality of neutrino Monte Carlo event generators, and thereby enhance the physics reach of many future experiments.

MINERνA will attack this problem from both experimental and theoretical directions. Experimentally, MINERνA will make definitive measurements of dozens of exclusive and inclusive cross-sections, across the range of energies most important for future oscillation and nucleon-decay experiments, with a well-controlled flux, and on a variety of nuclear targets. The era of 25% uncertainties and marginally-consistent cross-section data for even the simplest neutrino reactions will end with MINERνA; for the first time it will be possible to validate the details, and not merely the gross features, of competing models.

At the same time, MINERνA will be a natural focus of attention for theorists and phenomenologists developing these models. NEUGEN and NUANCE are two of the most sophisticated neutrino-physics simulations in the world, but NUANCE models quasi-elastic scattering with the 1972 calculation of Smith and Moniz[34], and both programs use the Rein–Sehgal[58] resonant production model which dates from 1981. That no other widely-accepted models for these, the most fundamental neutrino–nucleon reactions, have emerged in the last quarter century is sobering evidence that an experiment like

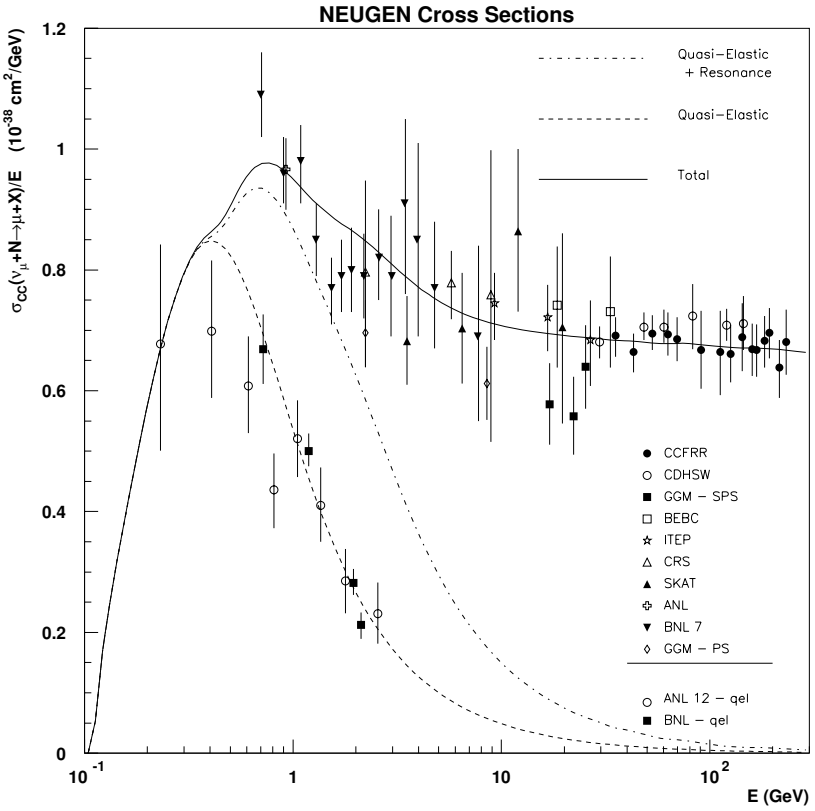

Figure 74: The NEUGEN prediction for the ν_μ charged-current cross-section (σ/E_ν) from an isoscalar target compared with data from a number of experiments. Quasi-elastic and resonance contributions are also shown.

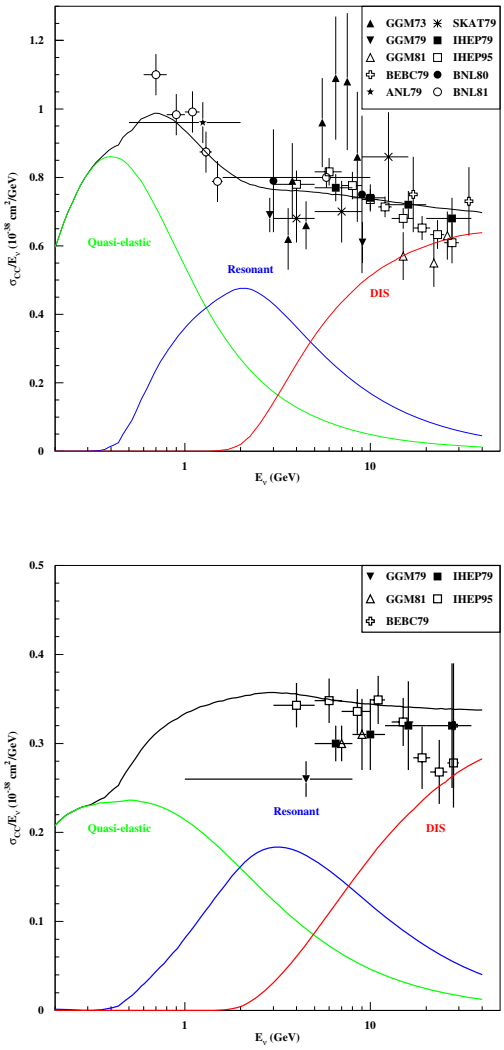

Figure 75: Total neutrino (top) and anti-neutrino (bottom) cross-sections divided by energy versus energy compared to the sum of quasi-elastic, resonant, and inelastic contributions from the NUANCE model. The sum is constructed to be continuous in W ($\equiv$ mass of the hadronic system) as follows. For $W > 2$ GeV the Bodek-Yang model is used. The Rein-Sehgal model is used for $W < 2$ GeV. In addition, a fraction of the Bodek-Yang cross-section is added to the Rein-Sehgal cross-section between $W = 1.7$ GeV and $W = 2$ GeV. The fraction increases linearly with W from 0 to 0.38 between $W = 1.7$ and $W = 2$ GeV.

MINERνA is long overdue. New, high-quality data is the surest way to catalyze theoretical ingenuity, and MINERνA will provide the former in abundance. Through our contacts with these theorists, and ability to translate well-tested, state-of-the-art models into universally-available and widely-adopted software, MINERνA will serve as a conduit for expertise from a diverse collection of disciplines into the high-energy neutrino physics community.[7]

11.2 Detector Response Simulation

Simulation of neutrino interactions in MINERνA is carried out by a GEANT3-based Monte Carlo program. This program combines a flexible description of the detector geometry, the NuMI neutrino beam flux from the beam simulation, neutrino interaction physics from either of the two generators and simulation of the scintillator response with the standard tracking and particle interaction routines available in GEANT.

11.2.1 GNuMI flux interface

The output of the GNuMI simulation of the beamline is a set of files recording the neutrino flux in 0.5 GeV bins for a nominal number of protons on target. The flux files are in a standard format and hence can be interchanged with no additional modifications to the code. In this way different beam configurations can be easily studied. An option exists to generate interactions with a flat energy spectrum. In this case, beam weights are stored in an output ntuple. This is particularly useful if one wishes to study the effect of different beam configurations without furthur Monte Carlo running.

11.2.2 Event generator interface

The Monte Carlo simulation program can be configured to accept neutrino interactions from either NEUGEN3 or NUANCE. The results of a neutrino interaction can be passed to the simulation in a number of ways. By default, the event generation routines in NEUGEN3 are usually called from within the simulation itself. In this mode, the code chooses a neutrino energy from the flux files, samples the density of material along the neutrino path; chooses a vertex and nucleus type, calls the kinematics generator and inserts the list of particles thus obtained into the GEANT data structures. This is not the only mode of generation. As a stand-alone generator, NUANCE provides events in either a text or ntuple format and so a provision is made to read in events from a standard external format. NEUGEN3 has been modified to write out events in the same format, so that the results of both generators may be compared in a consistent manner.

11.2.3 Geometry

Flexibility drives the design of the detector geometry code. The size, segmentation, material and shape of all components of the detector can be set and altered almost entirely from input datacards. The detector is logically divided into longitudinal sections. Each section can have different dimensions, strip sizes and absorber widths. In addition the absorbers in each section can be be constructed from

[7] This trend is already beginning, thanks to collaborative work sparked by the NUINT series of workshops. The BBA–2003 quasi-elastic form-factor fits (see Chapter 2) and Bodek–Yang duality-inspired model of deep-inelastic scattering (Section 6) have recently been implemented in NUANCE, and NEUGEN is exploring Benhar's spectral-function approach[172] to nuclear binding effects.

segments of differing material and widths. The geometry description is sufficiently abstract that minor changes in detector design may be accommodated merely by changing the datacard, allowing for fast detector reconfiguration and easy bookkeeping.

11.2.4 Hits and digitizations

Particles are tracked through the GEANT geometry in the standard manner. When a particle traverses a sensitive detector volume the particle type, volume identifier, entrance and exit points and energy deposition (including Landau and other fluctuations) are recorded as a hit. When GEANT has finished tracking the event, the hits are considered and converted to digitizations. There are as many digitizations as there are strips hit. Multiple hits on a single strip are condensed into one digitization, although information on which tracks contributed to the digitization is stored. These digitizations are then passed to the event reconstruction program.

11.2.5 Photon transport

The GEANT detector simulation assumes "ideal" light collection, and records the raw energy deposited in each channel. During event reconstruction, the energy deposited is converted to a number of detected photo-electrons. The scale factor between energy deposited and expected photo-electrons detected is determined by a standalone optical simulation validated for MINOS (see Section 11.3): the expected number of photo-electrons is smeared by Poisson statistics, and a 10% channel-to-channel Gaussian smearing reflecting a conservative estimate of remaining systematics after calibration and attenuation corrections.

11.3 Optical Simulation

MINOS has shown that co-extruded solid scintillator with embedded wavelength shifting fibers and PMT readout produces adequate light for MIP tracking and can be manufactured with excellent quality control and uniformity in an industrial setting. The performance characteristics of the MINOS scintillator modules produced at the three 'module factories' are now well known, both through measurements taking with radioactive sources post-fabrication at the factories and through measurements of cosmic rays at Soudan. We intend to use this same technology for the active elements of MINERνA.This section describes the light yield studies that were carried out in order to demonstrate that the proposed design produces enough light.

The basic active element in the MINERvA detector is a co-extruded triangular scintillator strip with a wave-length shifting fiber threaded through a small circular hole that runs through the middle of the strip. Like MINOS, the scintillator strips are polystyrene (Dow 663) doped with PPO (1 % by weight) and POPOP (0.03% by weight), co-extruded with a reflective coating of TiO_2 loaded polystyrene [174]. The strip cross-section is a triangle of width 3.3 cm and height 1.7 cm. Strip lengths vary throughout the detector and range from 1.4 meters to 2.2 meters in the inner tracking detector to 4 meters for the calorimeter sections. The WLS fiber (Kurrary Y11) is 1.2 mm in diameter. The WLS fibers are spliced to clear fibers which are mated to the PMT face. One ended readout is used, and the far strip/fiber end are mirrored.

Studies indicate that for a triangular extrusion, average light levels above 3.9 photo-electrons/MIP are required in the inner detector in order to obtain good particle identification (shown in Section 11.4.5). Coordinate resolution, vertex finding, and track pointing are also affected by light levels, but to a lesser

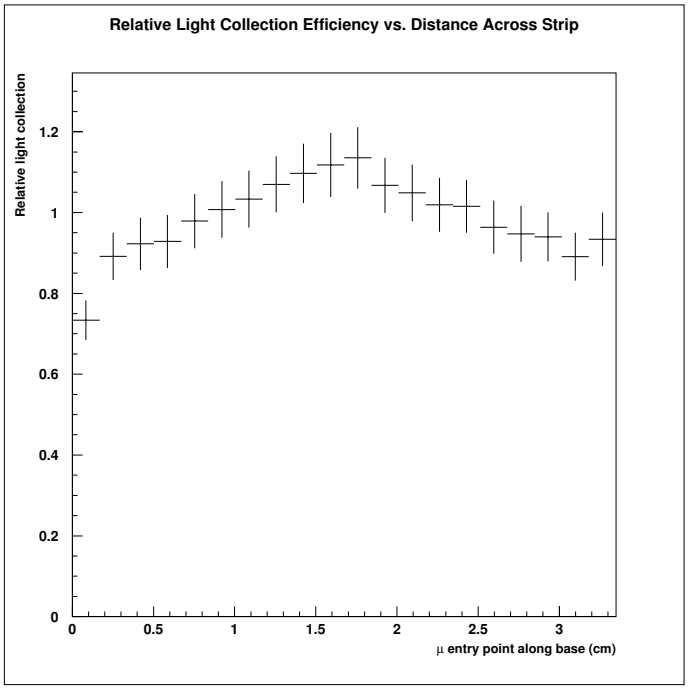

Figure 76: Relative light collection efficiency across the 3.35 cm triangular width of the scintillator extrusion.

extent. For this design we have targeted an average light level of 7.8 PE/MIP, which includes a safety factor of 100%. This safety factor accounts for some ad hoc assumptions in the simulations as well as possible effects from degradation of the scintillator over time.

The basic ingredients for the MINERvA light studies are the known characteristics of the MINOS modules and a photon transport Monte Carlo written by Keith Ruddick [165]. The average light yield from a MINOS scintillator module is 4.25 photo-electrons/MIP at a distance of 4 meters, and attenuation in the fiber is well described in terms of a double exponential: [173]:

$$\mathrm{N(x)} = \mathrm{A}(\exp(-\mathrm{x}/90\mathrm{cm}) + \exp(-\mathrm{x}/700\mathrm{cm})) \tag{14}$$

The photon transport Monte Carlo (LITEYLDX) is used to calculate, for a given 'configuration' (strip geometry, fiber diameter, and fiber placement), the number of photons trapped in the fiber for a MIP entering at a particular position. This information is then used to determine a relative light collection efficiency for a particular configuration compared to MINOS strips. With the overall normalization and attenuation curve from MINOS one can then calculate the amount of light for any particular configuration. Figure 77, for instance, shows the relative light output for triangular extrusions when the strip thickness, fiber diameter and fiber placement are varied. As expected, light output is nearly proportional to the strip thickness, and is greatest when the fiber is placed at the center of gravity of the strip. Figure 76 shows the relative light collection efficiency for a triangular extrusion where the entry point of the minimum ionizing particle is varied across the strip width, and indicates that the collection efficiency varies by $\pm 10\%$ over the strip width.

The overall light levels from 3 lengths of strips are shown in Figure 78. Here we have assumed a 90% reflectivity from the mirror end of the strip, and in all cases a 1 meter WLS 'pigtail' from the end

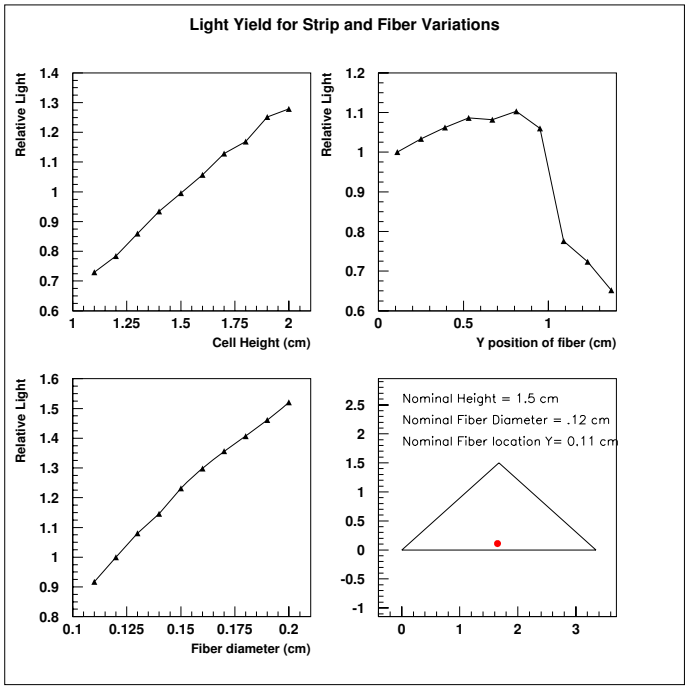

Figure 77: Relative light levels for different strip widths and fiber diameters.

of the near end of the strip to the PMT face. Clear fiber lengths and connectors are not included. In the MINOS near detector, the far strip end was not mirrored, here we assume the strip ends are mirrored with 100% reflectivity. Because the light produced in the scintillator is generally collected within a few cm of the MIP crossing location, this approximation only affects the calculation of collection efficiency at the very far end of the strip. Shown are the light levels predicted for 3 strip lengths. In each plot, the lowest curve corresponds to light collected from reflections off the mirrored end, the middle line corresponds to light travelling directly from the MIP to the readout end, and the upper line is the sum. As the figure shows, the light level in the inner tracking detector, with a maximum length of 2.2 m, meets the design requirement of 7.8 PE/MIP over the entire length.

11.4 Performance of Reconstruction Algorithms

The output of the detector simulation is a list of digitizations for each strip. We have developed a basic reconstruction program which takes this list and reconstructs the tracks and vertices in an event.

11.4.1 Pattern recognition

For our design studies, we have adopted "omniscient" pattern recognition based on Monte Carlo truth information. All hits generated by a given track (ignoring channels with overlap) are used to reconstruct the track. Development of a fully-realistic pattern-recognition algorithm to associate hits to track candidates has not been undertaken as yet due to manpower and time constraints. We are confident that the three-dimensional XUXV modular design of the detector, and its relatively modest occupancy, will allow highly-efficient pattern recognition and track identification. Visual inspection of events through

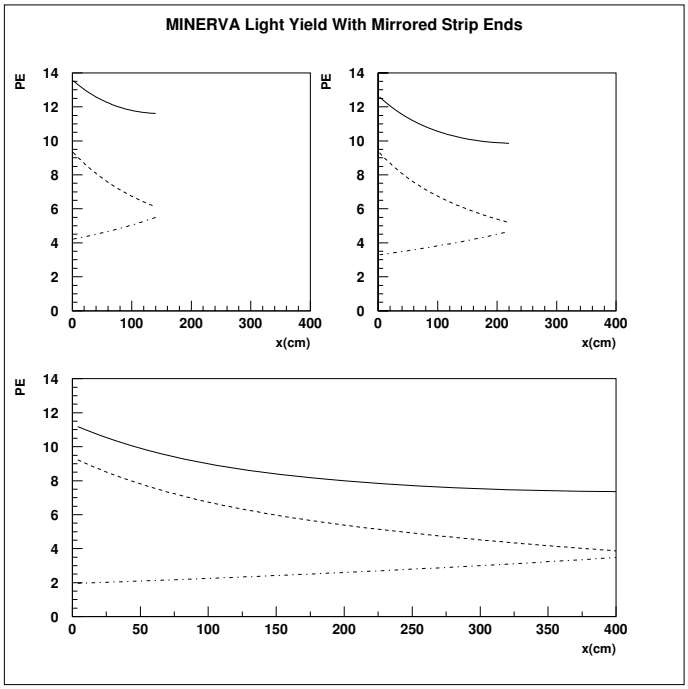

Figure 78: Light yield vs. distance along strip for MINERνA scintillator strips with one-ended readout with a mirrored end. Dot-dashed line is light collected from reflections off the mirrored end, dashed line is light travelling directly to the readout end; solid line is the sum.

the graphical interface of the detector simulation program reinforces this conclusion.

11.4.2 Coordinate reconstruction

Tracks generating hits in at least six scintillator planes of the inner detector, including three planes of the X view, can be reconstructed. Coordinates are estimated from the raw, smeared digitizations, using only planes which have one or two strips hit. Tracks at high angles to the detector axis may pass through more than two strips in a single plane, and it should be possible to recover these higher-multiplicity hits with a more sophisticated algorithm. For single hits, the coordinate is taken as the center of the strip. For dual hits, the position is interpolated using the charge-sharing between between strips, with a small geometrical correction based on the estimated crossing angle.

The coordinate resolution for a large test sample of single and double hits can be measured directly using the residuals obtained when each coordinate is excluded, in turn, from the track's fit. This coordinate resolution is parameterized as a function of the track's crossing angle, and used to assign errors to coordinates in the fitter.

11.4.3 Track reconstruction

Reconstructed coordinates are used to fit each track using a Kalman filter algorithm[175]. For this proposal, tracking performance has only been studied in the non-magnetic region of the detector; the track model is perforce a strictly linear one. Neglect of the magnetic field is justified because mission-critical

resolutions are determined by performance of the fully-active (non-magnetized) volume, and since coordinate resolution for the strips should not depend on the presence of a magnetic field. The momentum resolution for charged tracks in a magnetic field can be reliably estimated from the coordinate resolution, momentum and field strength. As long tracks may pass through many radiation lengths of scintillator and absorbing material, the Kalman filter's ability to correctly account for multiple Coulomb scattering ("process noise") is essential. The algorithm can optionally be used to exclude outliers from the fit.

Figure 79 shows the expected hit residuals, impact parameter and angular resolution for muons from a sample of quasi-elastic interactions, assuming triangular strips of 3 cm width and 1.5 cm thickness (close to the final design values). Hit resolutions of $\sim 3\,$mm and angular resolutions of $< 0.5^\circ$ are expected. The coordinate resolution is degraded to approximately 1.5 cm if rectangular strips are employed instead of triangular ones, since interpolation based on charge is no longer possible.

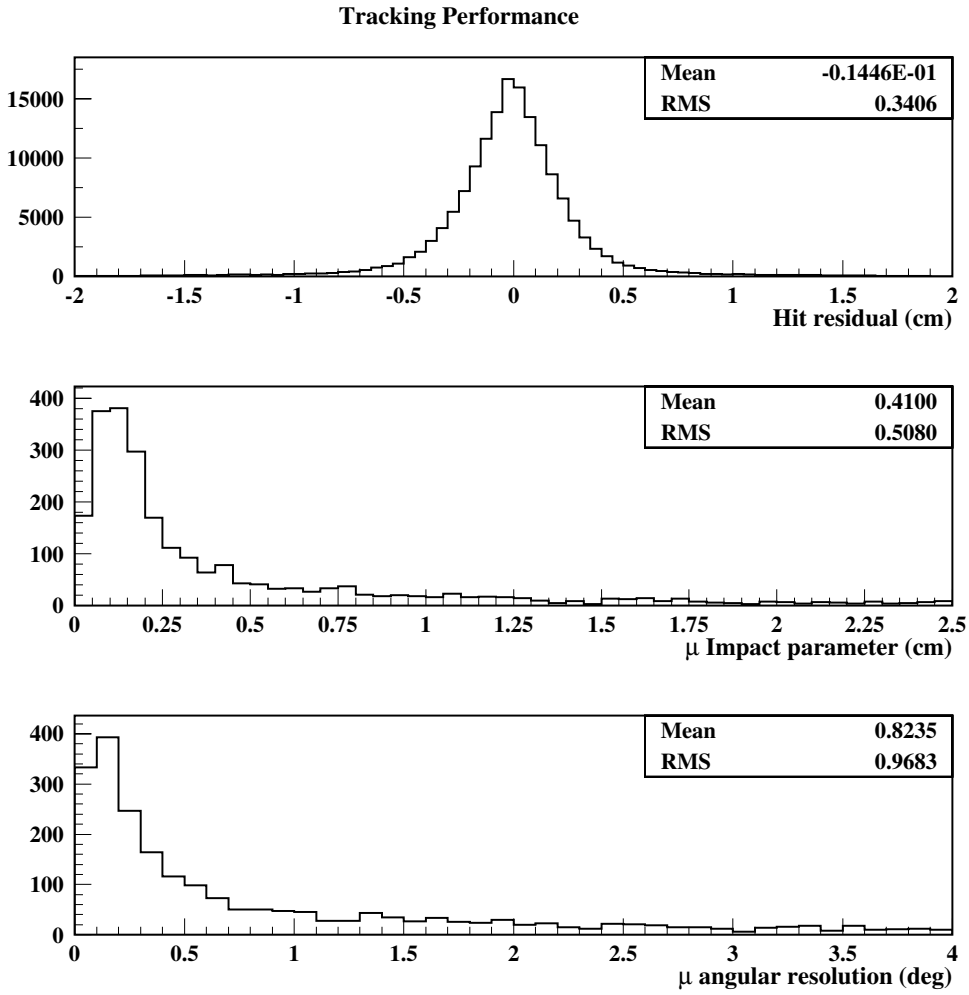

Figure 79: Performance of the tracking algorithm on muons from from a sample of simulated charged-current quasi-elastic interactions. Shown are (top) the hit residuals, (middle) the impact parameter of the muon with the vertex and (bottom) the muon angular resolution.

11.4.4 Vertex reconstruction

In this study, reconstructed tracks are associated to vertices using Monte Carlo truth information. The vertex positions are then fit using a Kalman filter algorithm. Track directions at the vertex are updated taking account of the constraint. This is equivalent to a least squares fit, but mathematically more tractable since it does not involve inversion of large matrices and can be easily extended to a helical track model. The primary vertex resolution for a sample of simulated quasi-elastic interactions with two visible tracks is shown in Figure 80. The transverse (longitudinal) vertex postion can be measured to a precision of better than (slightly more than) a centimeter.

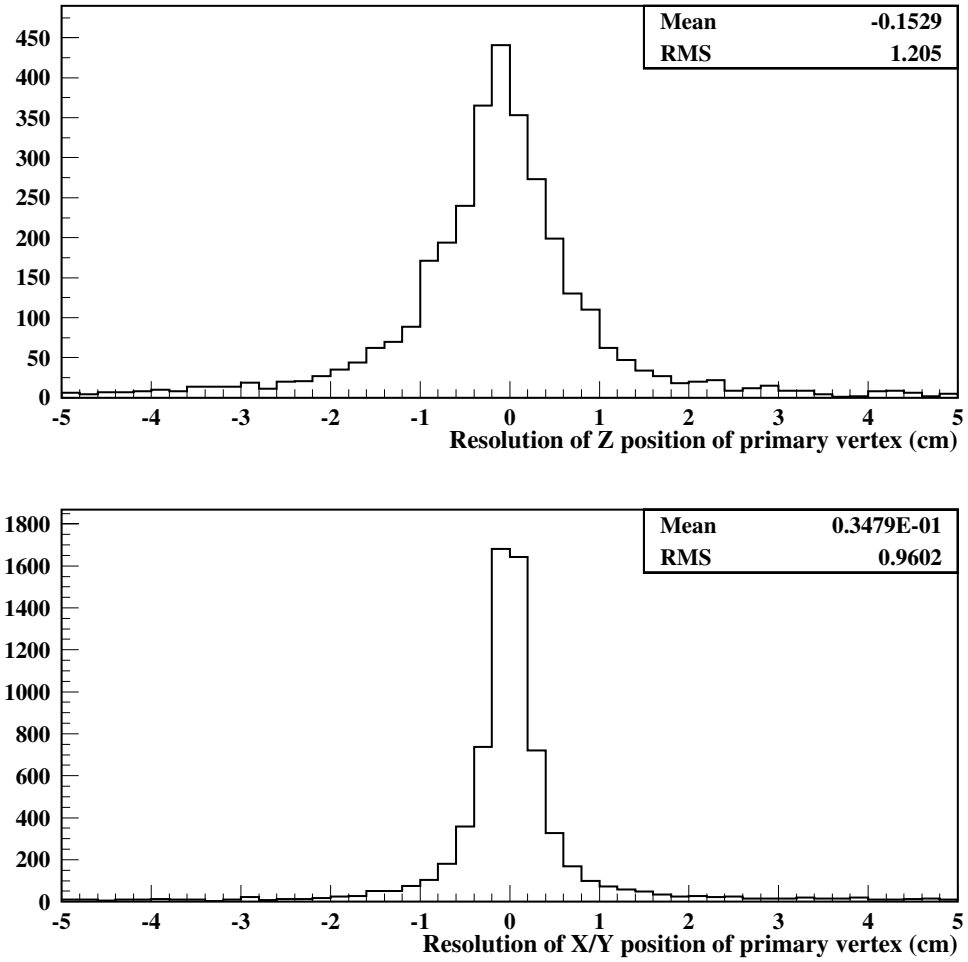

Figure 80: Reconstructed vertex resolution for two track charged current quasielastic events. Shown are (top) the resolution in the longitudinal position of the vertex (Z) and (bottom) the resolution of the transverse position of the vertex (X and Y).

11.4.5 Particle identification

Particle identification in MINERνA will rely on measuring specific energy loss (dE/dx) as well as topology (hadron and electromagnetic showers, decay signatures).

Electromagnetic showers Electromagnetic showers are easily identifiable by their diffuse track and characteristic dE/dx profile in the fully-active central detector and energy deposition in the electromagnetic calorimeters. In addition, the fine granularity of MINERνA allows us to distinguish electrons and photons, when the primary vertex is known, using distance to shower onset and shower length. Figure 81 shows the distance between the electromagnetic shower origin and the true primary vertex for charged-current ν_e interactions and π^0 production. The figure also shows the length of the showers, measured in MINERνA scintillator planes, or 1.75 cm of polystyrene. For neutral pions the length is from the beginning of the first showering photon to the end of the second one.

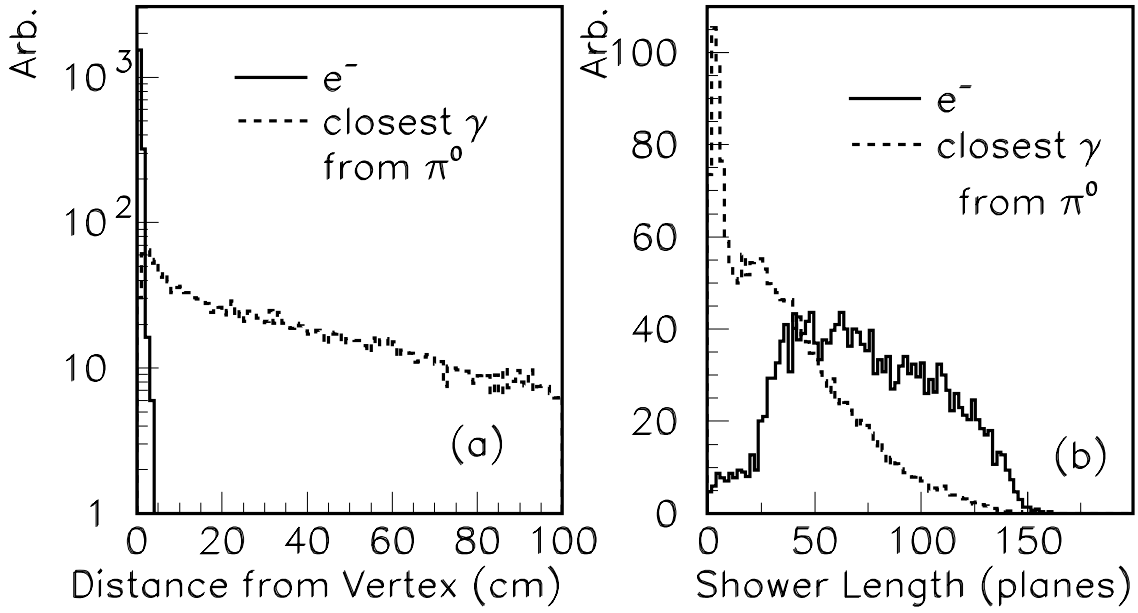

Figure 81: (a) The distance in centimeters between the neutrino vertex, which can be determined from a proton track, and the start of the most upstream electromagnetic shower, for both electrons and photons from neutral pions. (b) The shower length in units of scintillator planes, for electrons and neutral pions.

π^0 reconstruction With the surrounding ECALs for containment, MINERνA's π^0 reconstruction capabilities are excellent. This is essential, since π^0 are a major source of background for ν_e appearance oscillation experiments. As discussed in Section 3.3.3 and shown in Figure 14, MINERνA's low density and high granularity make it an excellent photon tracker, able to accurately reconstruct the vertex and kinematics even for coherently-produced π^0's with no accompanying charged tracks.

Muons Energetic muons can be identified by their penetration of material in the calorimeters and/or MINOS near detector. Muons with a momentum measurement in the magnetic field, or which stop inside the detector can be distinguished from protons and kaons by dE/dx. In addition, the delayed $\mu \to e$ decay signature can be detected.

Charged hadrons Hadrons can be identified as such by their interactions in the inner detector and/or hadron calorimeters. Hadrons which stop without interacting or have their momentum measured by the magnetic field can also be distinguished as π, K or p with good efficiency using dE/dx.

dE/dx analysis Specific energy loss (dE/dx) will be an important tool for particle identification in MINERνA. For tracks which stop in the inner detector, the charge deposited near the end of the track (corrected for sample length) can be compared with expected curves for, *e.g.,* the $\pi^{\pm}$, $K^{\pm}$ and proton hypotheses. This technique does not require an independent momentum measurement, since the range (x_{stop}, in g/cm^2) from the stopping point to a given sampling point is closely correlated with the momentum at the sampling point. The algorithm is calibrated by fitting the expected dE/dx vs. x_{stop}, and the standard deviation of this quantity, $\sigma_{dE/dx}$, as a function of x_{stop} for the three different particle types (see Figure 82). The measured dE/dx for a track is compared to the expected value at each sample, to form χ^2 estimators reflecting the goodness of fit to each of the three particle identification hypotheses:

$$\chi^2(\alpha) = \sum_{i=1}^{N_{sample}} \left[\frac{\left(\frac{dE}{dx}\right)_i^{obs} - \left(\frac{dE_\alpha}{dx}\right)_i^{exp}}{\sigma_i^\alpha} \right]^2 ,$$

where the sum runs over all measured samples, and $\alpha = \{\pi, K, p\}$. The hypothesis α with the minimum χ^2 is assigned to the track. The frequency of misidentification can be visualized most easily by plotting the difference $\Delta\chi^2$ between the correct χ^2 (for the particle's true type) and the smallest of the two (incorrect) others (Figure 83). With this naïve dE/dx analysis, MINERνA correctly identifies 85% of stopping kaons, 90% of stopping pions, and $> 95\%$ of stopping protons. A similar analysis can be applied to tracks with momenta measured in the magnetic regions of the detector.

11.4.6 Energy reconstruction and containment

Muons The energy of muons from charged-current interactions will be measured using range and/or curvature in the magnetized regions of MINERνA and the MINOS spectrometer. For muons stopping in the detector, the momentum resolution will be $\frac{\Delta p}{p} \sim 5\%$. If the MINOS detector is used, the momentum resolution will be 13%[152].

Electromagnetic showers For electromagnetic showers, the estimated energy resolution is $6\%/\sqrt{E(GeV)}$.

Hadronic calorimetry Containment of hadronic energy is a significant design consideration, as it assists in meeting many of the experiment's physics goals. Studies show that the visible hadronic component of quasi-elastic and resonant events in the fully-active central region of the detector are completely contained, apart from secondary neutrinos and low-energy neutrons. Figure 84 shows the fraction of escaping visible hadronic energy for deep-inelastic reactions in several hadronic energy ranges, and figure 85 shows the probability that a deep-inelastic event will leak visible energy as a function of the true hadronic energy. Only for hadronic energies greater than 8 GeV is there any significant probability of leakage and only above 15 GeV is the average fraction of escaping energy greater than 10%. The fraction of deep-inelastic interactions with hadronic energies over 15 GeV in the low-energy, semi-medium

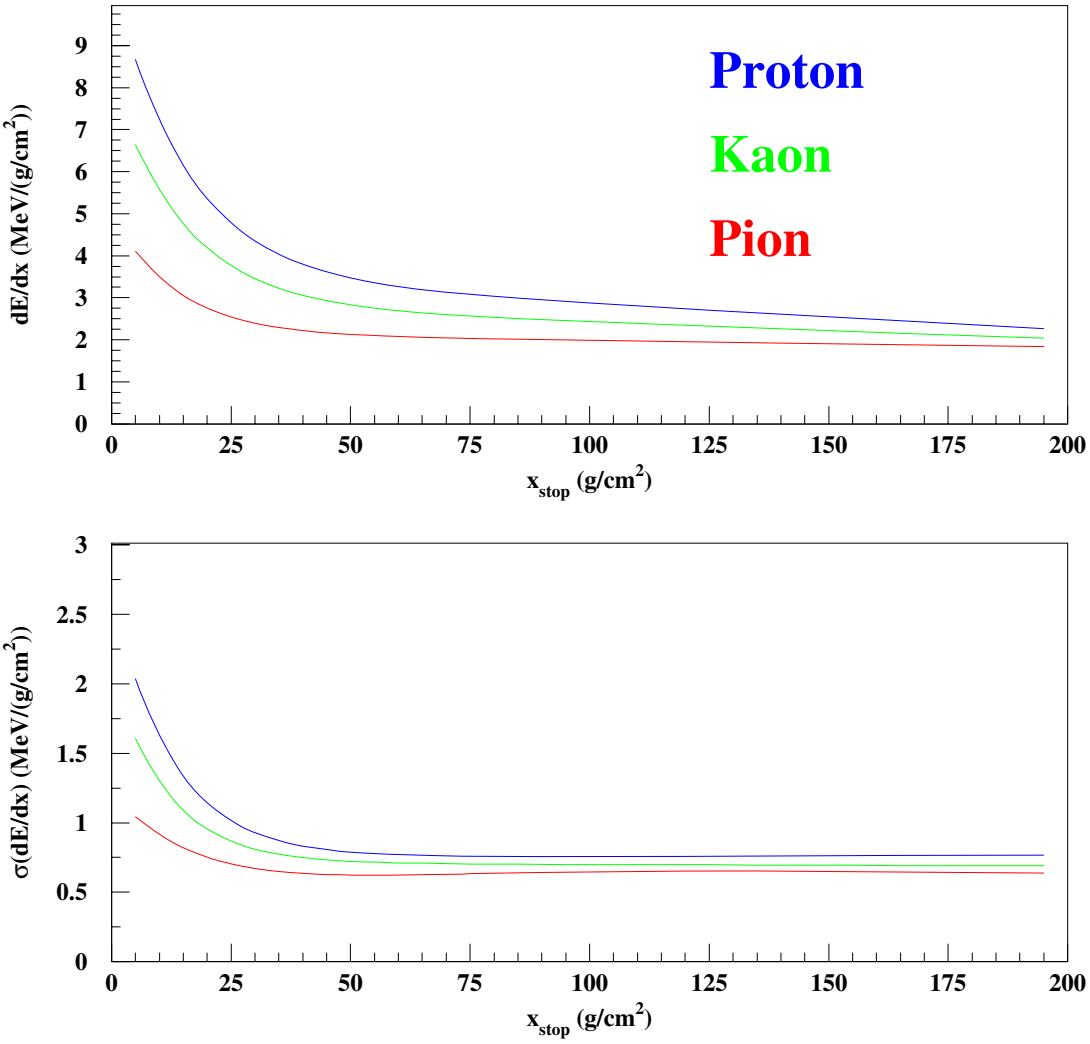

Figure 82: The top figure shows the average specific energy loss dE/dx for stopping $\pi^{\pm}$, kaons and protons, vs. range from the stopping point (in g/cm^2), for the simulated MINERνA inner detector. The bottom figure shows the estimated standard deviation of the energy loss, which is used to form a χ^2 estimator for particle identification.

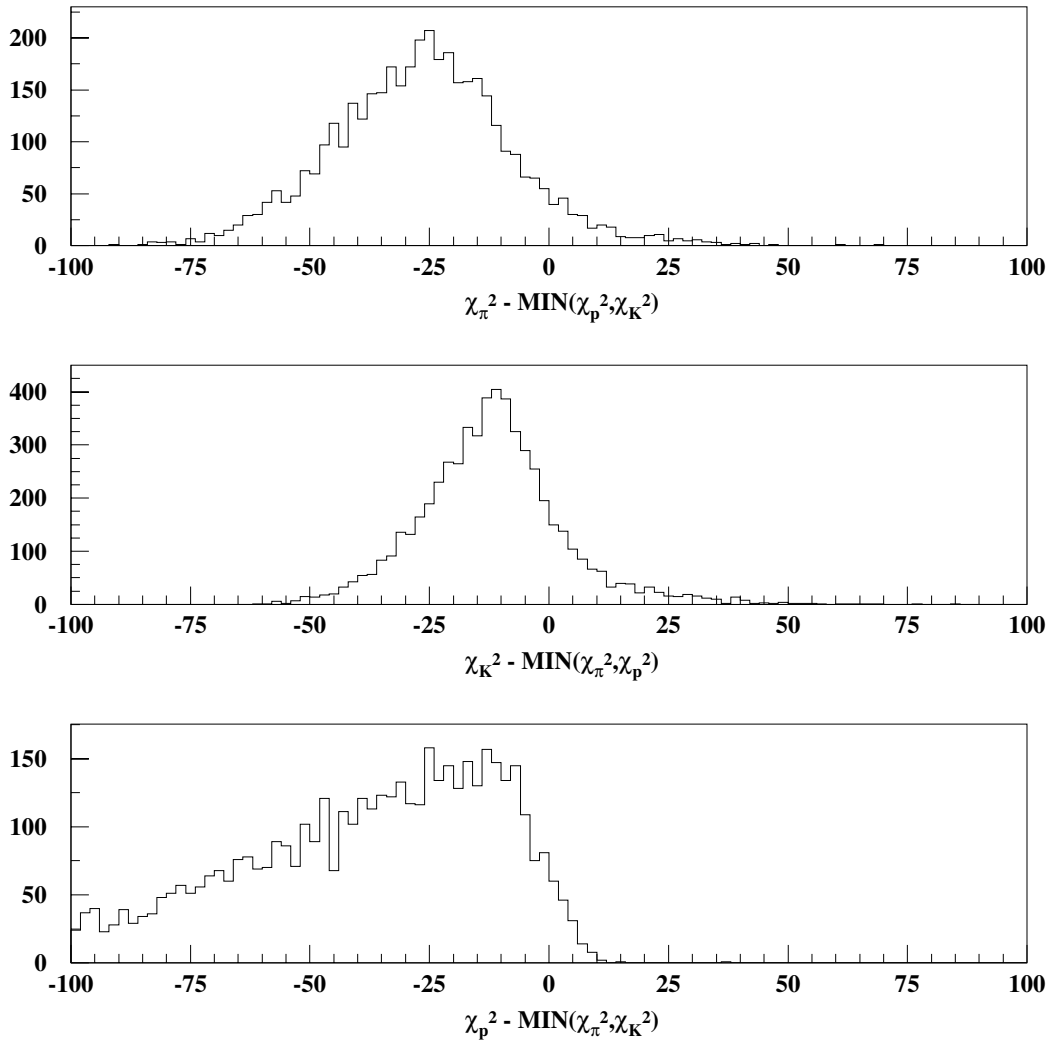

Figure 83: The three plots show the $\Delta\chi^2$ dE/dx estimator for simulated and reconstructed charged pions(top), kaons(middle) and protons(bottom) stopping in the inner detector. Tracks with $\Delta\chi^2 < 0$ are correctly identified.

or semi-high energy beams is $< 1\%$, and so visible energy leakage should be insignificant. These estimates ignore downstream components beyond the forward hadron calorimeter, such as the MINOS detector, and are therefore conservative.

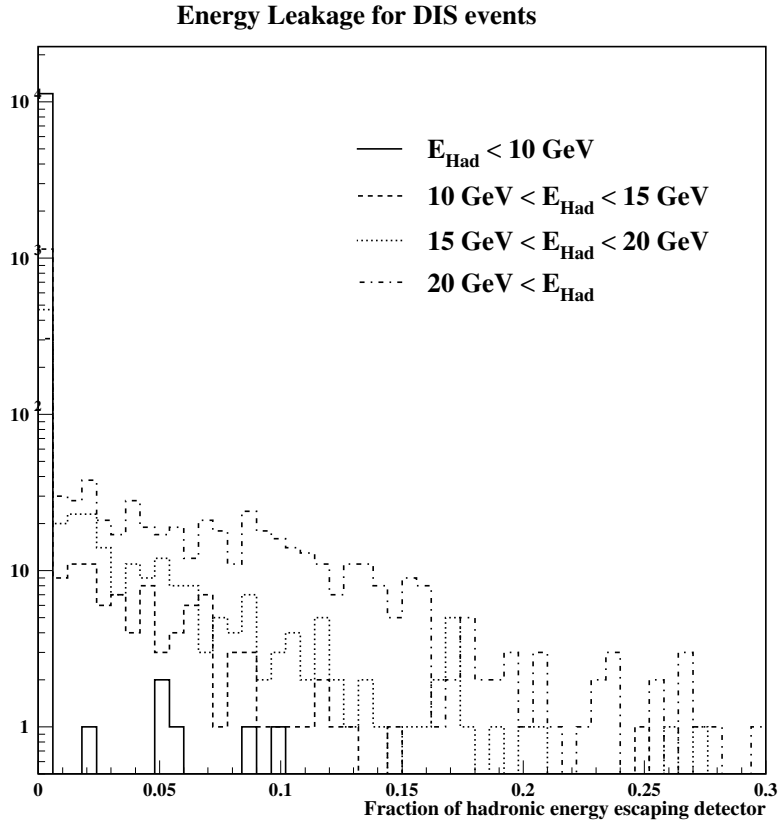

Figure 84: Fraction of hadronic energy escaping the detector for deep-inelastic scattering in the fully-active central region.

To study MINERνA's calorimetric E_h resolution, the detector response to a neutrino sample generated throughout the inner detector by NUANCE, on carbon and hydrogen targets, was simulated. From this simulated sample, events where all hadronic fragments were contained within MINERνA were used. Hits from lepton tracks in charged-current interactions are excluded from the following analysis.

In a fully-active scintillator calorimeter, the total light yield should be essentially proportional to E_h. (The proportionality is not unity due to escaping neutrinos, rest masses of charged pions, nuclear binding energy in the initial and secondary reactions and other nuclear effects such as pion absorption.) While the central inner detector volume is fully active, there are also regions with passive iron or lead absorber sandwiched between scintillators. In these sampling calorimeter regions, not all energy deposited results in scintillation light, so the light yield is corrected accordingly.

Figure 86 shows reconstructed E_h vs. true E_h computed from the kinematics of the incoming and outgoing leptons. The relative deviation of the reconstructed energy from the true E_h, $\Delta E_h/E_h$, multiplied by $\sqrt{E_h}$ is shown in figure 86, giving a average resolution for reconstruction of E_h of $\frac{\Delta E_h}{E_h} =$

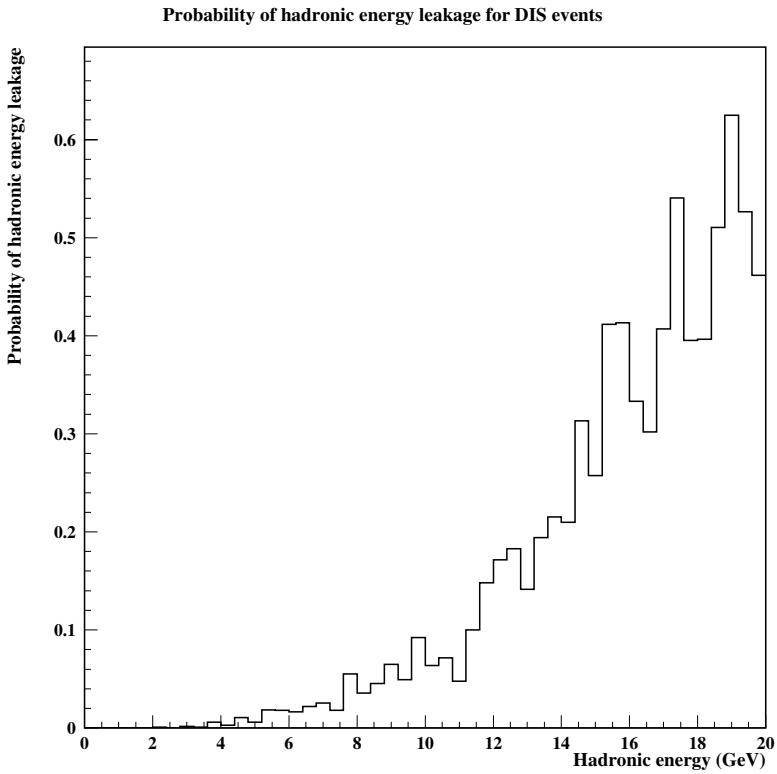

Figure 85: Probability that visible hadronic energy from a deep-inelastic event escapes undetected vs. total hadronic energy.

$\frac{23\%}{\sqrt{E_h(\mathrm{GeV})}}$. This $1/\sqrt{E_h}$ resolution has some energy dependence and is best represented by

$$\frac{\Delta E_h}{E_h} = 4\% + \frac{18\%}{\sqrt{E_h(\mathrm{GeV})}}.$$

11.4.7 Event categorization

Particle identification and event classification will play a central role in the analysis of data from MINERνA. One possible method of event classification is use of artificial neural network (ANN) techniques.

Event classification will be based on on topological characteristics as well as on particle ID. Separation of CC from NC interactions will be based on muon identification. Detection of muon decays for low energy muons stopping in the carbon gives the potential for accurate CC identification even at high y $_{Bj}$. In each such class further event identification will be based on other particle ID, energy/momentum measurements and kinematics. Neural networks are designed for such categorization and have been frequently used in the analysis of data from high energy physics experiments (see, for example, the DONUT[160] experiment).

11.5 R&D Studies

In Summer 2004, the collaboration began an extensive hardware R&D program in the following areas:

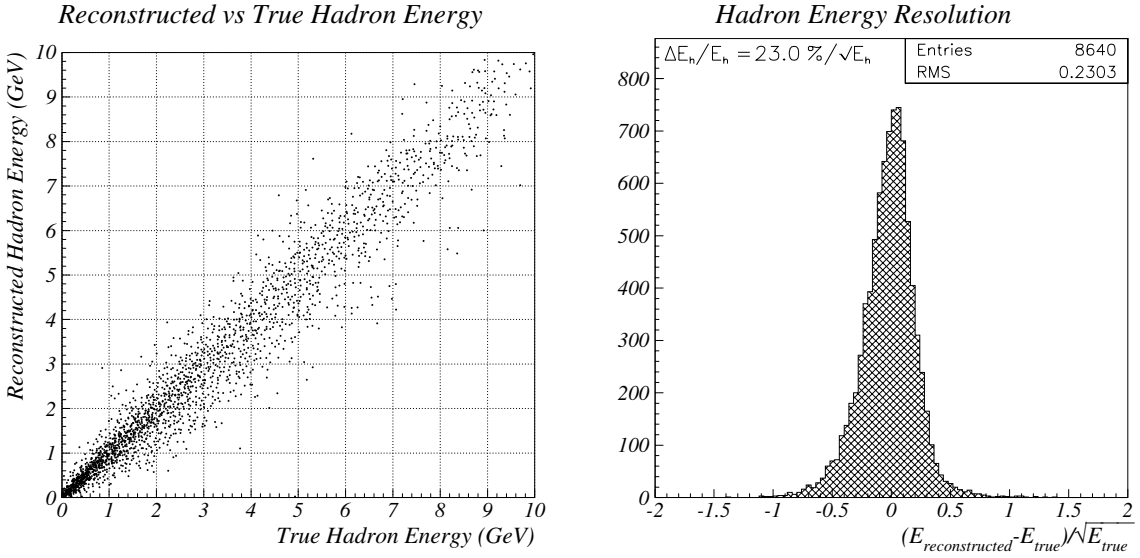

Figure 86: The left graph shows on the vertical axis the the hadronic energy E_h reconstructed from scintillator output in MINERνA vs. the true $E_h = E_\nu - E_\mu$. Right figure shows the relative deviation of the fit, $(\Delta E_h/E_h)\sqrt{E_h}$.

- Testing of triangular scintillator extrusion die
- Study of fiber optical and mechanical properties
- Development of a prototype front-end digitizer board (FEB)
- Tests of the FEB and scintillator system in a "Vertical Slice Test" (VST)
- Developing a scheme for the mechanical support of the planes of iron and scintillator bars
- Constructing and testing a full module (*XUXV* views) inner/outer detector prototype

Significant progress has already been made on the first four items, as discussed below. Preparations for the remaining tasks are underway.

11.5.1 Scintillator extrusions

Triangular scintillator prototypes have been produced using the NICADD/FNAL extrusion facility. Bars of the design dimensions have been successfully extruded, and a $\sim$1.5 mm hole through the center, for fiber insertion, has been integrated into the process. These test bars were used in the VST described below.

11.5.2 Optical fibers

MINERνA will use optical fiber for light collection. This fiber travels from the scintillator to the photosensor and must be bent along this path. Fibers were tested to study light loss and cracking at different curvatures, and determine the angle at which fibers can be safely bent in the mechanical design of the detector. The fiber tested was Y-11 (green) WLS S-35 J-type fiber, made by Kuraray, with 1.2- and 1.5-mm diameters.

Light loss in the fiber results from several effects: attenuation, geometric loss from bending, cracks, and optical coupling at the ends. These effects must be understood to select the appropriate fiber for the experiment.

Bending tests were performed in a dark box. A light mixer, which is a diffusing piece of plastic, was glued to a PMT and served to disperse the light from the fiber evenly before hitting the surface of the PMT. A R580-17 model 1.5 inch diameter PMT, made by Hamamatsu, was used for these tests. The other end of the fiber was fed into a tile. The tile is a $0.5 \times 4 \times 4$ in^3 piece of scintillator with a groove in the center of one of the broad sides. The broad ends of the tile were covered with Tyvek and the narrow sides were painted with white titanium dioxide paint. Grooved tiles with different diameters were used for tests with 1.2 and 1.5 mm fibers. The signal was generated by gamma decays from a 1.9 mCi Cesium-137 source, Compton scattering in the tile scintillator. The PMT current was measured with a picoammeter read-out by computer. For the bending tests, fiber was wrapped around cylinders with diameters ranging from 0.5 to 4.5 in, with the fibers making between 0.25 and 2 turns around the cylinder in different runs. Control fibers, prepared exactly like the fibers being tested, but not wrapped around the cylinder, were used to check the stability of the set-up. The results of the tests are summarized in the tables below.

	# of Wraps									
Diameter (in)	0	1/4	1/2	1	2	0 error	1/4 error	1/2 error	1 error	2 error
2	1.000	0.966	0.942	0.949	0.919	0.005	0.007	0.006	0.007	0.007
2.5	1.000	0.976	0.971	0.965	0.949	0.004	0.006	0.006	0.006	0.006
3.5	1.000	0.992	0.983	0.976	0.969	0.005	0.007	0.007	0.006	0.006
4.5	1.000	0.989	0.992	0.982	0.971	0.005	0.005	0.006	0.009	0.006

Table 12: Fraction of original signal surviving for different bend diameters, using 1.2 mm fiber.

	# of Wraps							
Diameter (in)	0	1/4	1/2	1	0 error	1/4 error	1/2 error	1 error
2	1.000	0.952	0.918	0.885	0.008	0.008	0.008	0.008
2.5	1.000	0.962	0.936	0.926	0.004	0.006	0.006	0.005
3.5	1.000	0.976	0.968	0.956	0.004	0.006	0.006	0.005
4.5	1.000	0.977	0.986	0.965	0.005	0.006	0.006	0.006

Table 13: Fraction of original signal surviving for different bend diameters, using 1.5 mm fiber.

While the 1.5 mm fiber gives higher light yield, it is much easier to break. Limits for minimum bend diameter can be set at 2 inches for the 1.2 mm fiber and 2.5 inches for 1.5 mm fiber. MINERνA plans to use the 1.2 mm fiber, unless it proves impossible due to lower light yield.

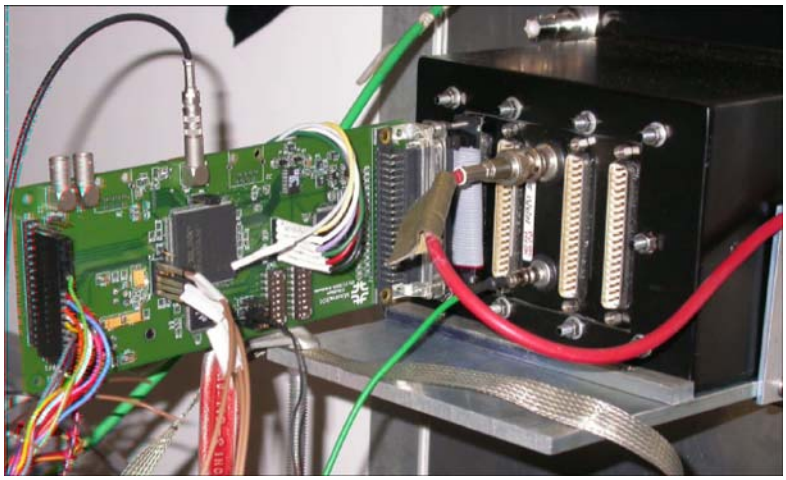

Figure 87: Photo of prototype readout board connected to a MINOS CalDet box.

11.5.3 Front-end prototype

A 16-channel FEB prototype, based on the TRiP chip, was designed and tested at FNAL. The essential elements are a TRiP chip (providing discimination, shaping, and an analog pipeline), high- and low-gain 10-bit ADCs, TDCs with 1.5 ns least-count, and an FPGA controller. Readout to the parallel port of a PC can be internally or externally triggered. On the bench, the board achieves the charge and timing resolution necessary for MINERνA. After commissioning and testing with pulser input, the prototype was used to read a real PMT as part of the vertical slice test (see Figure 87).

11.5.4 Vertical-slice test

To test the scintillator, front-end board and readout scheme, a small plane of the triangular bars were constructed at FNAL. Fibers from the bars were attached to a MINOS Near Detector M64 MAPMT housed in a MINOS CalDeT PMT box. Figure 88 shows a schematic of the VST set-up.

Single photo-electron and noise measurement The trigger for readout was either generated internally or by a set of scintillator paddles deployed above and below the prototype MINERνA plane to tag cosmic-ray muons. Tests of both these modes of operation proved successful. Using a blue LED flasher to excite the green fiber we were able to observe the single PE peak using this setup (Figure 89). The noise level, integrating over the nominal 10 μs NuMI spill time, was $<$2 fC (see Figure 90). This is much less than the measured charge of 30 fC from a single photo-electron using the lowest expected operating HV for the PMTs. Both high- and low-gain ADC channels were tested and functioned as expected.

The TDC channels where tested using the LED flasher by varying the time between the 10 μsec gate leading edge and the LED excitation pulse. The TDC values for the triggered channels displayed the expected linear response, with a time resolution better than 3 ns.

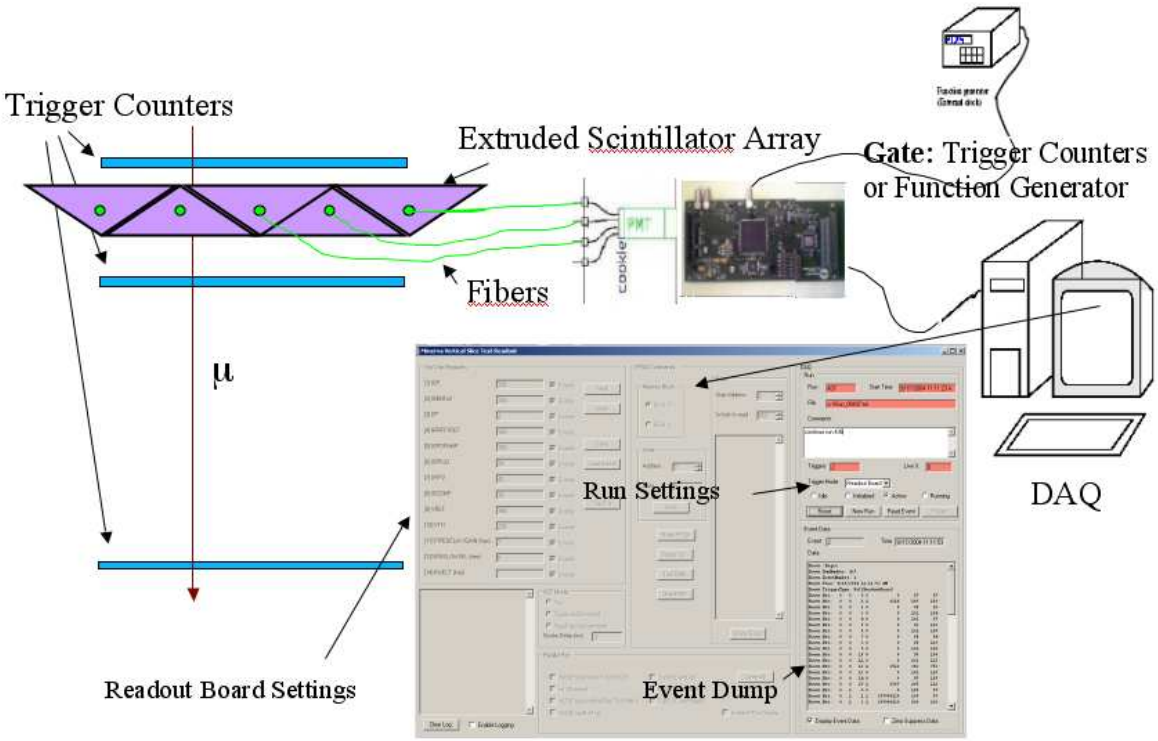

Figure 88: Schematic of vertical slice test set-up.

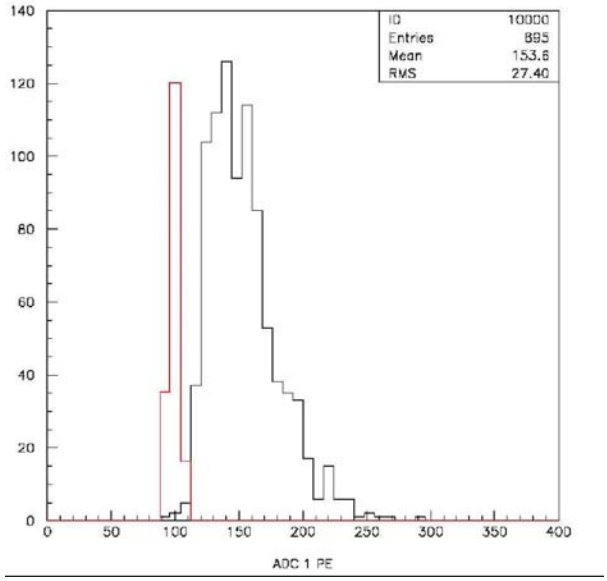

Figure 89: Single PE peak in high-gain ADC counts, measured with an LED pulser at very low occupancy. The pedestal peak in in red.

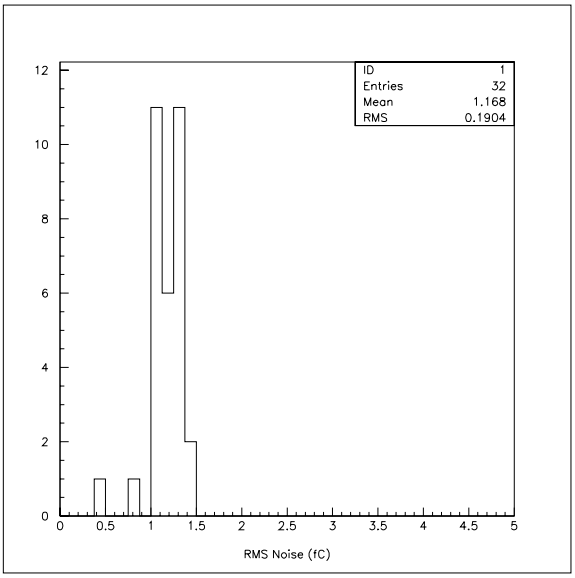

Figure 90: Pedestal RMS distribution for 32 ADC channels.

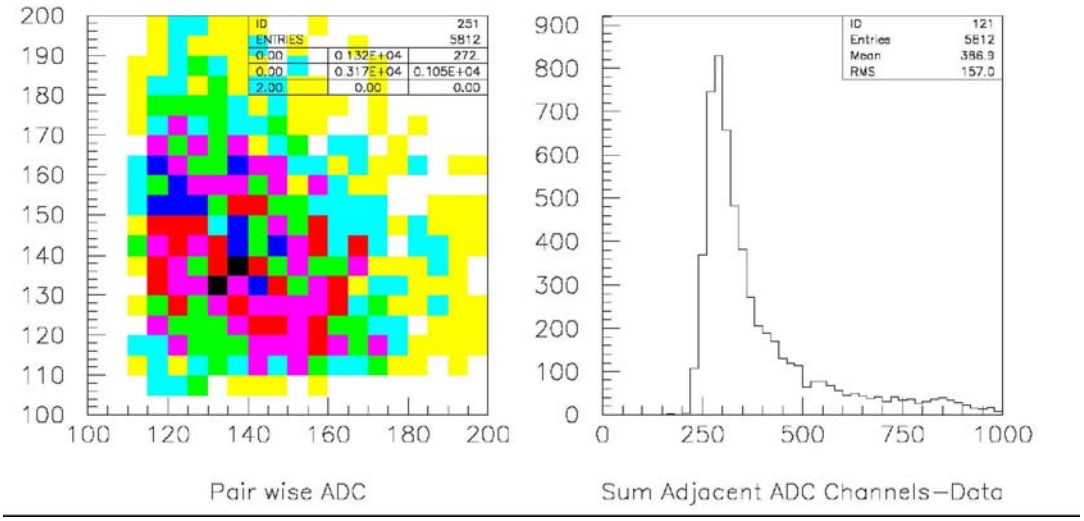

Figure 91: Left: Scatter plot of adjacent ADC counts for cosmic-ray muons. Right: Total light-yield for adjacent strips, using low-gain ADC channels.

Cosmic-ray muon light-yield Light yield from a single scintillator layer was measured using external triggers from cosmic ray muons. Vertical muons will excite two triangular scintillator strips in the layer, so anti-correlation between ADC values for adjacent channels is expected, and observed (Figure 91). The sum of adjacent ADC channels displays a clear peak and the expected tail from Landau variation and radiative energy loss. Combining the results of the single-PE and the cosmic ray measurements, the muon light-yield per layer is ~ 10 PE/layer for the light output.

For the real detector (after correcting for the different fiber lengths and an additional connector), these measurements imply a yield of ~ 7.5 PE/layer for minimum-ionizing particles. Note that VST measurements were performed with no optical coupling between the fibers and bars (air only). Based on MINOS studies, optical coupling should increase the light-yield by about a factor of two [176]. When this difference is accounted for, the measured light-yield agrees with predictions from the MINOS optical simulation (Section 11.3). The next round of measurements, in early 2005, will include optical coupling to confirm this agreement.

Part III
Bibliography

References

[1] Kamiokande Collaboration, S. Hatakeyama *et al.*, Phys. Rev. Lett. **81** (1998) 2016; Soudan-2 Collaboration, W. W. Allison *et al*, Phys. Lett. **B 449** (1999) 137; MACRO Collaboration, Ambrosio *et al*, Phys. Lett. **B434**, 451 (1998)

[2] Y. Fukuda et al., *Phys. Rev. Lett.* **81** (1998) 1158; Erratum **81** (1998) 4279, B.T. Cleveland et al., *Astrophys. J.* **496** (1998) 505. W. Hampel et al. (GALLEX Collaboration), *Phys.Lett.* **B 447** (1999) 127., J.N. Abdurashitov et al. (SAGE Collaboration), *Phys. Rev.* **C 60** (1999) 055801 [astro-ph/9907113]

[3] Q.R. Ahmad *et al.* Phys.Rev.Lett.**89** (2002) 011302 nucl-ex/0204009

[4] Y. Fukuda *et al.*, Phys.Rev.Lett.**81** (1998) 1562 [hep-ex/9807003]; M. Sanchez et al., Phys. Rev. **D 68**, 113004 (2003)

[5] KamLAND Collaboration (K. Eguchi et al.), Phys.Rev.Lett.**90** (2003) 021802 [hep-ex/0212021]

[6] K2K Collaboration (M.H. Ahn et al.), Phys.Rev.Lett.**90** (2003) 41801 [hep-ex/0212007]

[7] B. Pontecorvo and J. Exptl, Theoret. Phys. **34** 247 (1958); Z. Maki, M. Nakagawa and S. Sakata, Prog. Theor. Phys. **28**, 870 (1962).

[8] M. Maltoni *et al*, submitted to New J. Phys, [hep-ph/0405172]

[9] By CHOOZ Collaboration (M. Apollonio et al.), Phys.Lett.**B466** (1999) 415 [hep-ex/9907037]

[10] W. Grimus and L. Lavoura, Phys. Lett. **B572**, 189 (2003); A. Aranda, C.D. Carone, R.F. Lebed, Phys. Rev. **D62**, 016009 (2000).

[11] "A Long Baseline Neutrino Oscillation Experiment at Fermilab", E.Ables *et al*, FERMILAB-PROPOSAL-0875, Feb. 1995, 241pp.

[12] "NOVA: Proposal to build an Off-Axis Detector to Study $\nu_\mu \rightarrow \nu_e$ oscillations in the NuMI Beamline", I. Ambats *et al.*, FERMILAB-PROPOSAL-0929, Mar 2004.

[13] Y. Itow *et al*, "The JHF-Kamioka Neutrino Project", KEK report 2001-4, June 2001. [hep-ex/0106019]

[14] C.H. Llewellyn Smith, Phys. Rep. **3C** (1972).

[15] J. Arrington, nucl-ex/0305009.

[16] M. K. Jones *et al.*, Phys. Rev. Lett **84**, 1398 (2000); O. Gayou *et al.*, Phys. Rev. Lett **88**, 092301 (2002).

[17] H. Budd, A. Bodek and J. Arrington, To be published in *Proceedings of the Second Workshop on Neutrino-Nucleus Interactions in the Few-GeV Region (NUINT02),* Irvine, California (2002), arXiv:hep-ex/0308005.

[18] V. Bernard, L. Elouadrhiri, U.G. Meissner, J. Phys. **G28** (2002).

[19] G. Zeller (private communication).

[20] K. Tsushima, Hungchong Kim, K. Saito, nucl-th[0307013].

[21] T. Kitagaki *et al.*, Phys. Rev. **D26**, 436 (1983) .

[22] S. J. Barish *et al.*, Phys. Rev. **D16**, 3103 (1977).

[23] N. J. Baker *et al.*, Phys. Rev. **D23**, 2499 (1981).

[24] W.A. Mann *et al.*, Phys. Rev. Lett. **31**, 844 (1973).

[25] J. Brunner *et al.*, Z. Phys. **C45**, 551 (1990).

[26] M. Pohl *et al.*, Lett. Nuovo Cimento **26**, 332 (1979)

[27] L.B. Auerbach *et al.*, Phys. Rev. **C66**, 015501 (2002).

[28] S.V. Belikov *et al.*, Z. Phys. **A320**, 625 (1985).

[29] S. Bonetti *et al.*, Nuovo Cimento **38**, 260 (1977)

[30] K.L. Miller *et al.*, Phys. Rev. **D26** (1982) 537.

[31] H. Budd, A. Bodek and J. Arrington, [arXiv:hep-ex/0308005]; A. Bodek, H. Budd and J. Arrington, [arXiv:hep-ex/0309024] (to be published in Proceedings of CIPANP2003, New York City, NY 2003.)

[32] H. Budd, A. Bodek and J. Arrington, To be published in *Proceedings of the Third Workshop on Neutrino-Nucleus Interactions in the Few-GeV Region (NUINT04),* Laboratori Nazionali del Gran Sasso - INFN - Assergi(2004), arXiv:hep-ex/0410055.

[33] D. Casper, Nucl. Phys. Proc. Suppl. **112**, 161 (2002).

[34] R. A. Smith and E. J. Moniz, Nucl. Phys. **B43**, 605 (1972) ; E. J. Moniz *et al.*, Phys. Rev. Lett. **26**, 445 (1971); E. J. Moniz, Phys. Rev. **184**, 1154 (1969).

[35] Ghent Theory group in Belgium, Jan Ryckebusch (jan@inwpent5.UGent.be).

[36] G. P. Zeller, (2003), hep-ex/0312061.

[37] B. Z. Kopeliovich and P. Marage, Int. J. Mod. Phys. **A8**, 1513 (1993).

[38] D. Rein and L. M. Sehgal, Nucl. Phys. **B223**, 29 (1983).

[39] A. A. Belkov and B. Z. Kopeliovich, Sov. J. Nucl. Phys. **46**, 499 (1987).

[40] C. A. Piketty and L. Stodolsky, Nucl. Phys. **B15**, 571 (1970).

[41] E. A. Paschos and A. V. Kartavtsev, (2003), hep-ph/0309148.

[42] Super-Kamiokande and K2K, C. Mauger, Nucl. Phys. Proc. Suppl. **112**, 146 (2002).

[43] BooNE, J. L. Raaf, (2004), hep-ex/0408015.

[44] MiniBooNE, J. Monroe, (2004), hep-ex/0408019.

[45] K2K, T. Ishida, Prepared for 1st Workshop on Neutrino - Nucleus Interactions in the Few GeV Region (NuInt01), Tsukuba, Japan, 13-16 Dec 2001.

[46] B. Z. Kopeliovich, (2004), hep-ph/0409079.

[47] H. Faissner *et al.*, Phys. Lett. **B125**, 230 (1983).

[48] E. Isiksal, D. Rein, and J. G. Morfin, Phys. Rev. Lett. **52**, 1096 (1984).

[49] CHARM, F. Bergsma *et al.*, Phys. Lett. **B157**, 469 (1985).

[50] CHARM-II, P. Vilain *et al.*, Phys. Lett. **B313**, 267 (1993).

[51] BEBC WA59, P. P. Allport *et al.*, Z. Phys. **C43**, 523 (1989).

[52] BEBC WA59, P. Marage *et al.*, Z. Phys. **C31**, 191 (1986).

[53] SKAT, H. J. Grabosch *et al.*, Zeit. Phys. **C31**, 203 (1986).

[54] C. Baltay *et al.*, Phys. Rev. Lett. **57**, 2629 (1986).

[55] V. V. Ammosov *et al.*, Yad. Fiz. **45**, 1662 (1987).

[56] E632, S. Willocq *et al.*, Phys. Rev. **D47**, 2661 (1993).

[57] E. Paschos and A. Kartavtsev, Private Communication.

[58] D. Rein and L. M. Sehgal, Annals Phys. **133**, 79 (1981).

[59] D. Drakoulakos *et al.* MINERνA Collaboration, arXiv:hep-ex/0405002, pgs. 49 - 61, pgs. 201 - 210.

[60] E. A. Paschos, M Sakuda, J. Y. Yu, Phys. Rev. **D69**, 014013 (2004).

[61] G. M. Radecky *et al.*, Phys. Rev. **D25** 1161 (1982).

[62] T. Kitagaki *et al.*, Phys. Rev. **D34** 2554 (1986).

[63] M. Sakuda and E.A. Paschos, Nucl. Phys. B (Proc. Suppl.) **112** 89 (2002); M. Sakuda, http://www.ps.uci.edu/ nuint/slides/Sakuda.pdf

[64] R. Gran, To be published in *Proceedings of the Third Workshop on Neutrino-Nucleus Interactions in the Few-Gev Region (NUINT04),*

[65] N.J. Baker *et al.*, Phys. Rev. D **24**, 2779 (1981).

[66] A. Alavi-Harati *et al.*, Phys. Rev. **87** 132001 (2 001).

[67] P.G. Ratcliffe, Phys. Rev. **D59**, 014038 (1999).

[68] N. Cabibbo *et al.*, Semileptonic Hyperon Decay and CKM U nitarity, [arXiv:hep-ph/0307214] (July 2003).

[69] T. Alexopoulos *et al.* (KTeV Collaboration), Phys. Rev. Lett. **93**, 181802 (2004).

[70] T. Nakano *et al.*, [arXiv:hep-ex/0301020]; V.V. Barmin
em et al., [arXiv:hep-ex0304040]; S. Stepanyan [arXiv:hep-ex/0307018].

[71] R. Jaffe and F. Wilczek, Di-quarks and Exotic Spectroscopy, [ar Xiv:hep-ph/0307341] (July 2003).

[72] D. Drakoulakos *et al.* [Minerva Collaboration], fine-grained detector in the NuMI beam," arXiv:hep-ex/0405002. Pgs. 99 - 108, 192 - 200.

[73] B.Z. Kopeliovich, hep-ph/0409079.

[74] M.K. Jones *et al.*, Phys. Rev. **C48**, 2800 (1993); R.D. Ransome *et al.*, Phys. Rev. **C46**, 273 (1992); R.D. Ransome *et al.*, Phys. Rev. **C45**, R509 (1992).

[75] D. Rowntree *et al.*, Phys. Rev. **C60**, 054610 (1999); B. Kotlinksi *et al.*, Eur. Phys. J. **A9**, 537 (2000).

[76] E. A. Paschos, M. Sakuda, I. Schienbein and J. Y. Yu, arXiv:hep-ph/0408185.

[77] M. Arneodo, Phys. Rept. **240**, 301 (1994).

[78] G. Piller and W. Weise, Phys. Rept. **330**, 1 (2000).

[79] B. L. Ioffe, V. A. Khoze, and L. N. Lipatov, *Hard processes: Phenomenology, Quark-Parton Model* (Elsevier Science Publishers, North Holland, 1984).

[80] G.B. West, Ann. Phys. **74** (1972) 464.

[81] S. V. Akulinichev, S. A. Kulagin, and G. M. Vagradov, Phys. Lett. B **158**, 485 (1985); S. V. Akulinichev, S. Shlomo, S. A. Kulagin, and G. M. Vagradov, Phys. Rev. Lett. **55**, 2239 (1985).

[82] S. A. Kulagin, Nucl. Phys. A **500**, 653 (1989).

[83] C. Ciofi degli Atti and S. Liuti, Phys. Rev. C **41**, 1100 (1990).

[84] F. Gross and S. Liuti, Phys. Rev. C **45**, 1374 (1992).

[85] S. A. Kulagin, G. Piller and W. Weise, Phys. Rev. C **50**, 1154 (1994).

[86] S. A. Kulagin, W. Melnitchouk, G. Piller, and W. Weise, Phys. Rev. C **52**, 932 (1995).

[87] S. A. Kulagin, Nucl. Phys. A **A 640**, 435 (1998).

[88] W. Melnitchouk, A. W. Schreiber and A. W. Thomas, Phys. Rev. D **49**, 1183 (1994).

[89] J. Gomez, *et al.,* Phys. Rev. D **49**, 4348 (1994).

[90] S. I. Alekhin, S. A. Kulagin and S. Liuti, Phys Rev. D **69**, 114009 (2004).

[91] S. A. Kulagin and R. Petti, paper in preparation.

[92] T. H. Bauer, R. D. Spital, D. R. Yennie and F. M. Pipkin, Rev. Mod. Phys. **50**, 261 (1978) [Erratum-ibid. **51**, 407 (1979)].

[93] C. A. Pickety, and L. Stodolsky, Nucl. Phys. B **15**, 571 (1970).

[94] S. L. Adler, Phys. Rev. **135**, B963 (1964).

[95] R. J. Glauber, Phys. Rev. **100**, 242 (1955).

[96] V. N. Gribov, Sov. Phys. JETP **29**, 483 (1970) [Zh. Eksp. Teor. Fiz. **56**, 892 (1969)] ; Sov. Phys. JETP **30**, 709 (1970) [Zh. Eksp. Teor. Fiz. **57**, 1306 (1969)].

[97] B. Z. Kopeliovich, and P. Marage, Int. J. Mod. Phys. A **8**, 1513 (1993).

[98] S. A. Kulagin, arXiv:hep-ph/9812532.

[99] E. A. Paschos and L. Wolfenstein, Phys. Rev. D **7**, 91 (1973).

[100] G. P. Zeller *et al.* [NuTeV Collaboration], Phys. Rev. Lett. **88**, 091802 (2002) [Erratum-ibid. **90**, 239902 (2003)] [arXiv:hep-ex/0110059].

[101] S. A. Kulagin, Phys. Rev. D **67**, 091301 (2003) [arXiv:hep-ph/0301045].

[102] S. A. Kulagin, arXiv:hep-ph/0406220.

[103] S. A. Kulagin, arXiv:hep-ph/0409057.

[104] R. Merenyi *et al.*, Phys. Rev. D **45**, 743 (1992), W. A. Mann *et a l.*, unpublished.

[105] C.H.Q. Ingram, Nucl. Phys. A **684**, 122 (2001).

[106] M. K. Jones *et al.*, Phys. Rev. C **48**, 2800 (1993).

[107] M. Nakahata *et al*, Nucl. Instrum. Meth. **A421**, 113 (1999); E. Blaufuss *et al*, Nucl. Instrum. Meth. **A458** 638 (2001).

[108] M. Diwan and J. Nelson, NuMI-NOTE-STEEL-0639 (2000)

[109] PhD Thesis of C. Smith, University College London, London, 2002 *Calibration of the MINOS Detectors and Extraction of Neutrino Oscillation Parameters*; PhD Thesis of R. Nichol, University College London, London, 2003 *Calibration of the MINOS Detectors*

[110] PhD thesis of M. A. Kordosky, University of Texas at Austin, August 2004 *Hadronic Interactions in the MINOS Detectors*

[111] PhD thesis of P. L. Vahle, University of Texas at Austin, August 2004 *Electromagnetic Interactions in the MINOS Detectors*

[112] E. A. Paschos, L. Pasquali and J. Y. Yu, Nucl. Phys. B **588**, 263 (2000) and E. A. Paschos, J. Y. Yu and M. Sakuda [arXiv:hep-ph/0308130].

[113] D. Ashery *et al.*, Phys. Rev. **C23**, 2173 (1981).

[114] H. Gallagher, Nucl. Phys. Proc. Suppl. **112**, 188 (2002)

[115] NuMI Fluxes courtesy of Mark Messier

[116] The simulation assumed the active material was resistive plate chambers and the absorber was particle board (hydrocarbons).

[117] G.P.Zeller, submitted to proceedings of 2nd International Workshop on Neutrino - Nucleus Interactions in the Few GeV Region (NUINT 02), Irvine, California, 12-15 Dec 2002 [hep-ex/0312061]

[118] W. Melnitchouk, R. Ent, C.E. Keppel, accepted by Physics Reports.

[119] Sabine Jeschonnek and J.W. Van Orden, Phys. Rev. D **69**, 054006 (2004).

[120] F. E. Close and Nathan Isgur, Phys. Lett. B **509**, 81-86 (2001).

[121] R. Ent, C. E. Keppel, I. Niculescu, PRD **62**, 073008 (2000).

[122] I. Niculescu *et al.*, Phys. Rev. Lett. **85**, 1182-1185 (2000).

[123] C.E. Carlson and N.C. Mukhopadhyay, Phys. Rev. D **47**, 1737 (1993).

[124] F.E. Close and F.J. Gilman, Phys. Rev. D **7**, 2258 (1973).

[125] T. Abdullah and F.E. Close, Phys. Rev. D **5**, 2332 (1972).

[126] M. Diemoz, F. Ferroni, and E. Longo, Phys. Rev. **130**, 293 (1986).

[127] R. Belusevic and D. Rein, Phys. Rev. D **38**, 2753 (1988); Phys. Rev. D **46**, 3747 (1992).

[128] J. Arrington, R. Ent, C.E. Keppel, J. Mammei, and I. Niculescu, nucl-ex/0307012, submitted to Phys. Rev. Lett.

[129] SPIN0 ref

[130] G. R. Farrar and D. R. Jackson, Phys. Rev. Lett. **35**, 1416 (1975).

[131] KUHL ref

[132] U.K. Yang and A. Bodek, Phys. Rev. Lett. **82**, 2467 (1999).

[133] Lai:1994bb ref

[134] A. Bodek and U.K. Yang, Nucl. Phys. B (Proc. Suppl.) 112 70 (2002); Eur. Phys. J. **13**, 241 (2000).

[135] Gargamelletwist ref

[136] Varvell:1987qu

[137] J.C. Webb *et al.* [FNAL E866/NuSea Collaboration], hep-ex/0302019.

[138] See http://www.phys.psu.edu/∼cteq/ for a summary of CTEQ work; H. L. Lai *et al.* [CTEQ Collaboration], Phys. Rev. D **51**, 4763 (1995); H. L. Lai *et al.*, Eur. Phys. J. **12**, 375 (2000).

[139] V. A. Radescu *et al.* [NuTeV Collaboration].

[140] Jefferson Lab Experiment E03-012, approved.

[141] F.E. Close and W. Melnitchouk, Phys. Rev. C **68**, 035210 (2003); hep-ph/0302013.

[142] F.E. Close, F.J. Gilman, and I. Karliner, Phys. Rev. D **6**, 2533 (1972).

[143] F.E. Close and F.J. Gilman, Phys. Lett. B **38**, 541 (1972).

[144] X. Ji, Phys. Rev. Lett. **78**, 610 (1997).

[145] X. Ji, Phys. Rev. **D55**, 7114 (1997).

[146] A. V. Radyushkin, Phys. Lett. **B380**, 417 (1996).

[147] A. V. Radyushkin, Phys. Lett. **B385**, 333 (1996).

[148] J.C. Collins, L. Frankfurt, and M. Strikman, Phys. Rev. **D56**, 2982 (1997).

[149] A. V. Radyushkin, Nucl. Phys. **A711**, 99 (2002).

[150] M. Vanderhaeghen, Nucl. Phys. **A711**, 109 (2002).

[151] M. Diehl, hep-ph/0307382 (2003).

[152] MINOS Collaboration, "MINOS Technical Design Report", NuMI-NOTE-GEN-0337 (1998).

[153] N. V. Mokhov, "The MARS Monte Carlo", FERMILAB FN-628 (1995); N. V. Mokhov and O. E. Krivosheev, "MARS Code Status", FERMILAB-Conf-00/181 (2000); http://www-ap.fnal.gov/MARS/.

[154] N. Mokhov and A. Van Ginneken, J. Nucl. Sci. Tech. **S1**, 172 (2000).

[155] M. Messier (private communication)

[156] Y. Hayato, To be published in *Proceedings of the Second Workshop on Neutrino-Nucleus Interactions in the Few-GeV Region (NUINT02),* Irvine, California (2002).

[157] G. Ambrosini *et al.* [NA56/SPY Collaboration], Eur. Phys. J. C **10**, 605 (1999).

[158] P-907: Proposal to Measure Particle Production in the Meson Area Using Main Injector Primary and Secondary Beams, May 2000

(http://ppd.fnal.gov/experiments/e907/Proposal/E907_Propsal.html)

[159] NuMI Technical Design Handbook

(http://www-numi.fnal.gov/numiwork/tdh/tdh_index.html)

[160] K. Kodama *et al.*, Nucl. Phys. Proc. Suppl **98**, 43-47 (2001)

[161] E. Gallas & J. Li., "Polishing Optical Fibers for the D0 ICD in Run II", FNAL-TM-2062, 1998.

[162] P. de. Barbaro, et. al., "Quality Control Studies of Scintillating Tile/Fiber Megatile Productin for the CDF End Plug Upgrade Hadron Calorimeter", UR-1371/ER40685-821, CDF Note 2778.

[163] N. Pearson (Minnesota), private communication.

[164] D. Michael (CalTech) and T. Chase (Minnesota), private communication.

[165] K. Ruddick (Minnesota), private communication.

[166] J. Grudzinski (Argonne), private communication.

[167] N. Tagg, et al., "Performance of Hamamatsu 64-anode photomultipliers for use with wavelength–shifting optical fibres," NuMI-PUB-SCINT 1040, [physics/0408055].

[168] The MINERνA Collaboration, "*Proposal to perform a high-statistics neutrino scattering experiment using a fine-grained detector in the NuMI beam*", Fermilab Proposal P-938, e-print hep-ex/0405002; see Sect. 16.5.2.

[169] "MCM II and the Trip Chip", J. Estrada, C. Garcia, B. Hoeneisen and P. Rubinov, August 2002, FERMILAB-TM-2226.

[170] J.K. Nelson, "The MINOS Magnets", DPF2000, NuMI-703, August 2000.

[171] J.K. Nelson, J. Kilmer, "Overview of the design of the MINOS Near detector Coil," NuMI-L-523, August 1999;
J. Kilmer, R.W. Fast, R. Currier, and R. Stanek, "Specifications for Aluminum Conductor," NuMI-L-411, September 1998;
A. Lee, private communication.

[172] O. Benhar, [arXiv:nucl-th/0307061].

[173] L. Mualem (private communication).

[174] MINOS Collaboration, P. Adamson *et al.*, IEEE Trans. Nucl. Sci. **49**, 861 (2002).

[175] R. Fruhwirth, Nucl. Inst. Meth. **A262**, 444 (1987).

[176] "Studies of Extruded Plastic Scintillator for MINOS", Karol Lang and Todd Soesby, NuMI-NOTE-L-250, Feb 1997.